Materials Today Physics 39 (2023) 101273

Contents lists available at ScienceDirect

Materials Today Physics

journal homepage: www.journals.elsevier.com/materials-today-physics

Engineering metalenses for planar optics and acoustics

Beomseok Oh [a,1], Kyungtae Kim [a,1], Dongwoo Lee [a,1], Junsuk Rho [a,b,c,*]

[a] Department of Mechanical Engineering, Pohang University of Science and Technology (POSTECH), Pohang, 37673, Republic of Korea
[b] Department of Chemical Engineering, Pohang University of Science and Technology (POSTECH), Pohang, 37673, Republic of Korea
[c] POSCO-POSTECH-RIST Convergence Research Center for Flat Optics and Metaphotonics, Pohang, 37673, Republic of Korea

ARTICLE INFO

Keywords:
Metasurface
Metalens
Optical metalens
Acoustic metalens
Imaging system

ABSTRACT

Metalens, a two-dimensional planar system composed of strategically engineered subwavelength structures, facilitates precise manipulation in the process of both light and sound. Benefiting from the synergy between theoretical exploration and cutting-edge fabrication in the past decade, metalenses have attracted considerable attention owing to their thin structure and large number of degrees of freedom. Herein, we comprehensively review recent developments in optical and acoustic metalenses. Initially, we provide an overview of the fundamental principles and design perspectives of metalenses. Subsequently, we discuss the current challenges affecting planar optical and acoustic technologies. Then, we introduce emerging applications that leverage the capabilities of metalenses. Finally, we summarize this review with a discussion of various perspectives to guide future works.

1. Introduction

Understanding the five fundamental human senses is undoubtedly essential. Among these senses, sight and hearing play active roles in interacting with waves. For instance, object shapes are recognized by interpreting visible light reflecting off them, while audible sound facilitates inter-person communication through oscillations in media. Remarkably, these interactions between waves and matter extend beyond the visible and audible spectrum, and they have practical applications in various methods, such as X-ray and ultrasound inspections.

Efforts to harness wave-shaping have led to the development of diverse components. In optics, for example, important optical components such as lenses, prisms, and mirrors have contributed substantially to various functionalities of microscopes, telescopes, cameras, displays, and lithography technologies [1–3]. However, the associated intricate manufacturing process and inherent material constraints have made it challenging to achieve finely curved surfaces and optimal component quality, resulting in system complexity and aberrations.

Meanwhile, on the acoustic side, diverse devices such as microphones, loudspeakers, and absorbers, play indispensable roles. In particular, ultrasonic transducers and curvilinear lenses are employed to shape airborne sounds used for beamforming and sensing, and their use extends to waterborne and ultrasound applications [4–7]. Given that these components require electronic circuits with signal processing and bulk systems a few practical limitations need to be solved. In the context of sound-absorbing materials [8–10], adherence to the mass density law [11] introduces limitations in terms of using higher thickness to achieve effective absorption, particularly at lower frequencies. Although considerable progress has been made, certain limitations remain, warranting further research.

A metasurface is a two-dimensional (2D) wave manipulator that has capabilities for modulating the amplitude, phase, and polarization of waves, via tailor-made arrangements of subwavelength structures called meta-atoms. The concept of using subwavelength structures to manipulate waves has been employed for quite some time [12–14] and has garnered attention in both optics and acoustics over the past decade. It has led to the implementation of a planar system capable of replacing traditional bulk components such as beam-steering, focusing, and absorption [15–18]. Furthermore, it has paved the way for the development of novel wave manipulators that can be extended to intriguing applications, such as holograms [19], molecular barcoding [20], analog computing [21], drug delivery [22], wireless communication [23], and extreme ultraviolet light guiding [24].

In this review, we address recent challenges and advancements in metalens technology in optical and acoustic domains. The roadmap is as follows: we start with a concise overview of the design principles of

* Corresponding author. Department of Mechanical Engineering, Pohang University of Science and Technology (POSTECH), Pohang, 37673, Republic of Korea.
E-mail address: jsrho@postech.ac.kr (J. Rho).
[1] These authors contributed equally to this work.

https://doi.org/10.1016/j.mtphys.2023.101273
Received 11 September 2023; Received in revised form 19 October 2023; Accepted 25 October 2023
Available online 3 November 2023

metalenses. Then, we introduce the current challenges, including high-numerical aperture (NA) implementation, aberration correction, and achieving broadband operation. Moreover, we highlight the advances in tunability and multifunctionality, and describe emerging applications. Finally, we summarize our discussion and provide an outlook for the future.

2. Design principles

2.1. Fundamentals of electromagnetic and acoustic wave physics

Theories of light have drawn inspiration from analogies with sound. In the 17-th century, Robert Hooke speculated that light was a form of *vibrating motion* within a medium through which it traveled at a finite speed (later, it was found that no medium was required for light propagation) [25,26]. Moving forward to the 19-th century, Maxwell and Lord Kelvin extensively employed physical and mathematical parallels between electromagnetism and acoustics. The visco-elastodynamic equations can be modified so that they closely resemble Maxwell's equations. This analogy establishes a mathematical equivalence that allows us to interpret wave phenomena in both domains using the same analytical approaches [25,27].

Acoustic waves are longitudinal *scalar* waves in fluids or gases. The fundamental field equations can be expressed in terms of particle velocity $v(t, r)$ and acoustic pressure $p(t, r)$ with two constitutive parameters, ρ and κ (mass density and bulk modulus, respectively), which are listed in Table 1. By contrast, electromagnetic waves are transverse *vector* waves with two polarizations, characterized by electric and magnetic fields ($\mathbf{E}(t, r)$ $\mathbf{H}(t, r)$, respectively). These waves are governed by Maxwell's equations, which are also outlined in Table 1, and involve two constitutive parameters, ε and μ (permittivity and permeability, respectively). The speeds of sound and light are expressed as $c = \sqrt{\kappa/\rho}$ and $c = \sqrt{1/\epsilon\mu}$, respectively. The duality within these constitutive parameters can be readily comprehended, where pairs in distinct domains can be mutually correlated, such as $\rho \leftrightarrow \varepsilon$ and $1/\kappa \leftrightarrow \mu$. This suggests that acoustic and electromagnetic waves have a significant overlap in their underlying physics, explaining why advancements in electromagnetic metamaterials have progressed alongside developments in their acoustic counterparts [28]. We note that the characteristics of a metasurface can be understood by its effective wave speed along the propagation direction, which is related to its effective refractive index n_{eff} or phase delay $\phi = n_{\text{eff}}kd$, where k is the wavevector and d is the thickness of the slab [29]. In particular, considering that unit cells are generally much smaller than the wavelength of interest, the entire structure (i.e., metasurface) can be considered a homogeneous medium with effective material characteristics. This implies that we can control the response of light and sound by tailoring their constitutive properties to our needs. From a mathematical viewpoint, two physical domains share the wave equation $\nabla^2\psi = \frac{1}{c^2}\frac{\partial^2\psi}{\partial t^2}$, where ψ can represent variables such as p in acoustics or $\mathbf{E}$ and $\mathbf{H}$ in electromagnetism. In Table 1, we summarize the main quantities of acoustic and electromagnetic field theory.

In what follows, we begin by describing the conventional approach for designing metalenses, known as local phase modulation, and then shift our attention to the non-local phase modulation strategy.

Table 1
Duality between electromagnetism and acoustics.

	Electromagnetism	Acoustics
Governing equations	$\nabla \times \mathbf{E} = -\mu\frac{\partial \mathbf{H}}{\partial t}$	$\nabla p = -\rho\frac{\partial \mathbf{v}}{\partial t}$
	$\nabla \times \mathbf{H} = \epsilon\frac{\partial \mathbf{E}}{\partial t}$	$\nabla\cdot\mathbf{v} = -\frac{1}{\kappa}\frac{\partial p}{\partial t}$
	$\nabla\cdot\mathbf{E} = 0, \nabla\cdot\mathbf{H} = 0$	
Constitutive parameters	ε, μ	ρ, κ
Wave equation	$\nabla^2\psi = \frac{1}{c^2}\frac{\partial^2\psi}{\partial t^2}$	
Wave speed	$\sqrt{\frac{1}{\epsilon\mu}}$	$\sqrt{\frac{\kappa}{\rho}}$

2.2. Local phase modulation

In traditional components, a gradual phase accumulation occurs as the wave propagates through curved bulk lenses to form a spherical wavefront that converges at the focal point. By contrast, when a wave passes through a metasurface, it undergoes an abrupt phase shift induced by subwavelength structures. These structures introduce local phase changes, thereby facilitating precise control over the trajectories of light and sound through modulation of the material properties, dimensions, and compositions of individual meta-atoms. One fundamental principle in metasurface design involves mapping the desired phase profile using the generalized Snell's law and allocating meta-atoms that fulfill the transmission and local phase shift requirements relevant to the spatial domain. In this approach, all meta-atoms are designed independently, without taking into account nearest neighbor interactions, i.e., each meta-atom operates in a decoupled manner. In an implementation of a metasurface as a single-wavelength lens, for example, a bundle of rays should converge at the focal point through constructive interference. This is achieved by placing meta-atoms that correspond to the well-known hyperbolic phase profile as follows:

$$\phi(x, y) = \frac{2\pi}{\lambda}\left(f - \sqrt{f^2 + x^2 + y^2}\right), \tag{1}$$

where λ is the wavelength, f is the focal length, and x and y are in-plane positions.

In optics, three categories of meta-atoms are mainly used to manipulate the local phase of light: propagation phase, geometric phase, and resonant phase. In the propagation phase, which is characterized by its pillar-shaped configuration, a meta-atom can serve as a truncated waveguide and cause phase retardation. The phase retardation effect relies on the height and effective index of the nanopillars [30]. In general, this mechanism is polarization-independent and has a high efficiency. The geometric phase, called the Pancharatnam–Berry (PB) phase, affords control over circularly polarized light. For example, when the geometric phase of a meta-atom is used in conjunction with an anisotropic metablock, an incident wave is decomposed into its co-polarized and cross-polarized components. With this approach, complete phase modulation of its cross-polarized components can be realized by simply rotating the metablocks while maintaining a uniform structure [31]. The resonant phase is another avenue for phase manipulation, and it can be exploited through various physical phenomena, such as localized surface plasmon resonance, Fabry–Pérot resonance, and Mie resonance [32–34]. Although this phase offers narrow bandwidth, a low aspect-ratio design can yield significant benefits from the fabrication perspective.

In the acoustic domain, three representative toy models commonly used in acoustic metamaterials for local phase modulation are zig-zag structures, hybrid resonating structures, and phononic crystals (PCs). A zig-zag structure effectively elongates the propagation path of waves [35–38]. Within this coiled space, waves undergo phase retardation; therefore, these structures can be used in both transmission- and reflection-type metasurfaces [39–41]. This approach is suitable for controlling the effective refractive index through space squeezing, thereby allowing downsizing to subwavelength dimensions. Hybrid resonating structures, which comprise Helmholtz resonators and a straight waveguide, have been introduced as an alternative approach. The Helmholtz resonator, with its neck and cavity, functions as an equivalent mass–spring system that facilitates phase modulation through impedance tailoring and the waveguide acts as an impedance matcher, enabling efficient energy transfer to achieve the desired functionalities [42–44]. PCs are constructed using wave scatterers, and they offer advantages in achieving broad bandwidth [45–49]. Through a

periodic arrangement of inclusions with a high contrast in impedance compared to those of the host medium, PCs can form a bandgap within the desired frequency spectrum. While wave propagation is effectively suppressed within these bandgaps, various types of wavefront-shaping can be implemented using the effective properties obtained from non-dispersive responses at lower frequencies below the bandgaps. For example, when the constitutive parameters change gradually, a gradient index (GRIN) medium that provides wave-focusing capabilities can be obtained [50–52]. The toy models in optics and acoustics are depicted in Fig. 1C.

2.3. Nonlocal phase modulation

As previously discussed, in the context of local phase modulation, it is postulated that each meta-atom operates independently. However, subwavelength meta-building blocks are inherently bound to *sense* each other, exhibiting both weak and strong couplings, leading to nonlocal effects (Fig. 1B). In the case of strong interactions between adjacent elements, nonlocal metasurfaces possess intriguing behaviors [57]. For example, they offer a new degree of freedom that was once considered a nuisance, resulting in enhanced performance (e.g., efficiency, Q-factor) and new functionalities that have attracted significant attention in recent years for sophisticated imaging and signal processing, such as near-field imaging, high-NA focusing, bandpass filters and edge detection [57–61].

In optics, nonlocal metasurfaces have been advanced through two emerging concepts: quasi-bound states in the continuum (quasi-BICs) and guided-mode resonance (GMR) for the manipulation of light with wavelength selectivity, leading to the realization of high-Q metasurfaces (Fig. 1D). Quasi-BICs have been proposed and validated for effectively manipulating light across multiple degrees of freedom, resulting in high-Q resonance and free space coupling by introducing perturbations to break the symmetry of the BICs [54,62,63]. This approach can be applied to nonlocal phase-modulated metalenses [54,63]. Moreover, interesting studies have proposed the incorporation of GMR into metagratings to efficiently couple with the desired channel, featuring a high-Q factor [53,64,65]. By incorporating periodic notches into nanobars, where the period matches the guided mode wavevector, momentum coupling with the external field is enabled, leading to the excitation of GMR and a specific narrow spectral response [53].

In acoustics, two prominent concepts are employed in nonlocal acoustics. The first concept involves establishing a direct connection between adjacent unit cells, facilitating the *tunneling* of acoustic energy across a metasurface, resulting in strong coupling between neighboring meta-atoms. For example, waveguides interconnected by additional bridges (Fig. 1D) serve as fundamental structural elements [55] for harnessing nonlocality within acoustic metasurfaces. Moreover, nonlocality can be achieved in other structures, such as Helmholtz resonators and zig-zag configurations, all grounded in the same fundamental principle. These structures can be mathematically interpreted according to the combination of their local acoustic impedances, irrespective of their geometric complexity [66]. The second concept is based on the coupling effects induced by mutual acoustic radiation, referred to as radiation coupling, and it can be used for metagratings (Fig. 1D) [56]. Interestingly, nonlocal metagratings with radiation coupling inherently comprise a "gain" region that emits acoustic energy and a "loss" region that absorbs energy. This mutual energy exchange gives rise to nonlocality [67]. Ultimately, nonlocal effects enable extreme wave manipulation, which cannot be achieved with the local phase modulation regime, e.g., perfect reflection without leakage, highly efficient beam steering, asymmetric transmission, and high-NA wave focusing [68].

For more comprehensive literature reviews regarding the evolution of non-local photonic and acoustic metasurfaces, readers are encouraged to consult Refs [57,61,68,69].

2.4. Material choice

In optics, material properties exhibit strong wavelength dependence. Therefore, it is crucial to select the appropriate materials for metalens design and fabrication. The key factors guiding material choice include refractive index, extinction coefficient and fabrication complexity [70]. Metals such as aluminum (Al), silver (Ag), and gold (Au) are primarily utilized for plasmonic or reflective metalenses owing to their inherent reflection and ohmic loss, particularly in the ultraviolet (UV) to near-infrared (NIR) region. By contrast, transmissive metalenses are predominantly composed of dielectric materials. In the visible range, materials such as titanium dioxide (TiO_2) [31], gallium nitride (GaN) [71] amorphous silicon (a-Si) [72], and crystalline silicon (c-Si) [73] are commonly employed, benefiting from their high refractive index and convenience of fabrication. Recently, low-loss hydrogenated amorphous silicon (a-Si:H) has been proposed, offering advantages in terms of fabrication [74].

Notably, there is an increasing demand for UV metasurfaces in various fields, including high-resolution spectroscopy, lithography, biomedics, and quantum optics [75]. However, available materials face limitations due to their absorption of high-energy photons, necessitating narrow meta-atom periods to satisfy the Nyquist–Shannon sampling theorem. Consequently, high refractive index and large-bandgap materials, such as silicon nitride (SiN_x) [76], niobium pentoxide (Nb_2O_5) [77], aluminum nitride (AlN) [78], and hafnium oxide (HfO_2) [79], are employed for meta-atoms. Recently, a zirconium dioxide (ZrO_2) nanoparticle-embedded resin (nano-PER) metahologram, replicable through nanoimprint lithography, was demonstrated at 248 nm [80].

Acoustic metamaterials, in contrast to their optical counterparts, are primarily characterized by the geometry of their structure rather than the base materials of which they are composed. These metamaterials often employ materials with high acoustic impedance. For instance, in airborne acoustic metamaterials, common materials include engineering plastics such as polymethylmethacrylate (PMMA), polylactic acid (PLA), acrylonitrile butadiene styrene (ABS), and polyvinyl alcohol (PVA). In underwater applications, metals such as Al, steel, and titanium are predominantly chosen owing to their relatively high acoustic impedance, resulting in near-rigid boundary conditions. This emphasis on geometric design and high-impedance materials highlights the distinctive characteristics of acoustic metamaterials compared to their optical analogs. The advancements in additive manufacturing technologies, particularly three-dimensional (3D) printing methods have facilitated the production of meta-building blocks at a small scale (subwavelength) with high printing resolution, ensuring the creation of intricate acoustic components.

3. Challenges and progress

Over the past decade, metalenses have undergone significant advancements [81–84]. In particular, remarkable capabilities in terms of achieving monochromatic focusing with an ultra-thin flat platform have been demonstrated successfully, thereby distinguishing metalenses from conventional systems. However, despite the remarkable progress, various challenges persist, such as reducing aberrations, enhancing efficiency, and achieving broadband operation capability. Addressing these challenges is crucial for realizing the integration of metalenses into real-world applications. In what follows, we comprehensively discuss the current progress and challenges, elucidating on the road ahead for photonic and acoustic metalens technology.

3.1. Optical perspective

3.1.1. High numerical aperture

In an ideal lens, waves converge at an infinitesimally small point. However, the diffraction pattern arising from a circular aperture imposes limitations on the ability to distinguish between two light sources,

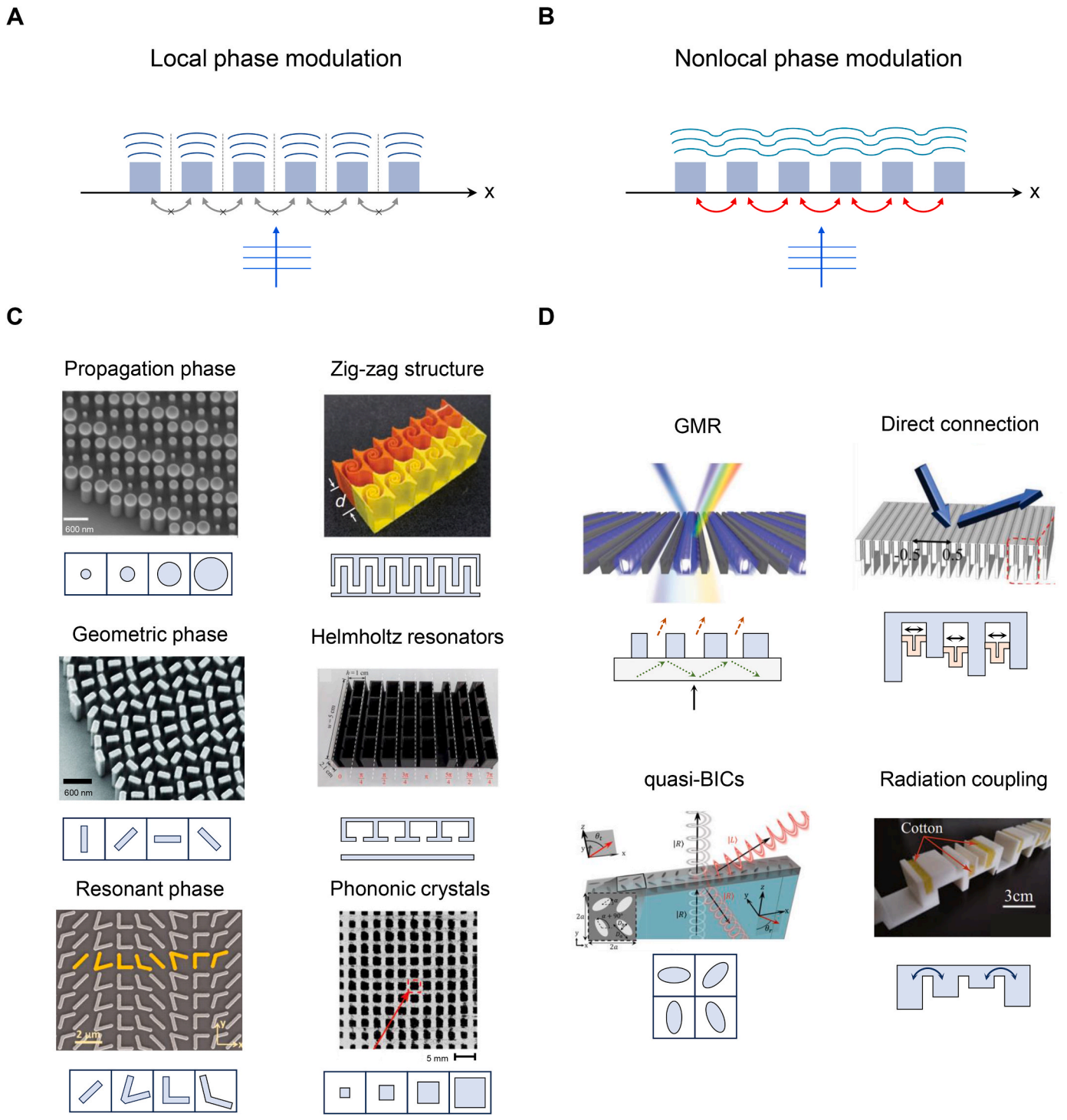

Fig. 1. Design principles of metasurfaces. Schematic of (A) local phase and (B) nonlocal phase modulation. (C) Representative optical and acoustic meta-building blocks. Propagation phase meta-atom (scanning electron microscopy [SEM] image), reproduced with permission from [30], copyright 2016 American Chemical Society, geometric phase meta-atom (SEM image), reproduced with permission from [31], copyright 2016 American Association for the Advancement of Science, and resonant phase meta-atom (SEM image), reproduced with permission from [32], copyright 2016 American Association for the Advancement of Science, zig-zag meta-atom, reproduced with permission from [38], copyright 2014 Springer Nature, Helmholtz-resonator array-type meta-atom, reproduced with permission from [43], copyright 2015 American Physical Society, and PC-type meta-atom, reproduced with permission from [50], copyright 2020 American Physical Society. (D) Basic mechanisms of nonlocal optical and acoustic metasurfaces: GMRs, reproduced with permission from [53], copyright 2020 Springer Nature, quasi-BICs, reproduced with permission from [54], copyright 2020 American Physical Society, direct connections, reproduced with permission from [55], copyright 2019 American Physical Society, and radiation-induced coupling effects, reproduced with permission from [56], copyright 2021 Springer Nature.

affecting the resolution. This resolution is closely linked to the NA of the lens, which characterizes its capacity to capture and focus the wave. The formula for the NA of the lens is classically defined as follows

$$\mathrm{NA} = n\sin\left(\tan^{-1}\frac{D}{2f}\right), \tag{2}$$

where n is the refractive index of the medium, D is the diameter of the lens, and f is the focal length of the lens. In this context, a high-NA metalens can be designed by substituting a small focal length or large diameter in eq. (2). However, spherical aberration still exists, and the focusing efficiency of metalenses can decrease unless the arrangement of meta-atoms complies with the Nyquist–Shannon sampling theorem in the spatial domain, as expressed $p \leq \frac{\lambda}{2\mathrm{NA}}$ [85], where p is the period of the unit cell. This formula indicates that p should be small enough to address spherical aberration for high-NA metalenses. However, it may lead to unwanted coupling effects between individual meta-atoms and pose challenges in a fabrication process employing high aspect ratio meta-atoms with high refractive index materials to ensure perfect 2π phase coverage [86]. Moreover, it is crucial to ensure that the lens operates effectively across all regions, particularly at the periphery, where high spatial frequencies are represented. This can be further specified by comparing the point spread function (PSF), Strehl ratio, and modulation transfer function (MTF) with the diffraction-limited case.

Persistent endeavors to achieve high-NA metalenses have been pursued through advanced approaches. In one such study, a metalens with an impressive NA of 1.48 was realized using a conventional immersion technique and an optimization algorithm to determine the optimal nanobrick dimensions. The optimized length, width, height, and center-to-center spacing of the c-Si meta-atom were determined using algorithms in terms of the hyperbolic phase profile and transmission. The characteristics of the fabricated metalens at a wavelength of 532 nm included NA values of 0.98 and 1.48 and focusing efficiencies of 67 % and 48 % in air and oil, respectively (Fig. 2A) [73]. High-NA metalenses can alternatively be realized using the inverse design approach, which is used to solve problems through mathematical optimization [87–90]. Using this strategy, a metalens with an NA of 0.94 based on the adjoint optimization has recently been reported [89]. Fig. 2B shows the schematic of the optimization procedure. The parameters of meta-atoms are updated iteratively by calculating the gradient of the figure of merit (FOM) in a two-step simulation involving forward and adjoint simulations until the FOM converges. The optimized metalens achieved a focusing efficiency of 49 %, which is 13 % higher than that of the conventional periodic unit-cell metalens. Interestingly, metagratings are promising for the fabrication of high-NA metalenses. Metagratings involve the precise arrangement of scatterers within a supercell to redirect incident waves to the desired deflection angles with both superior efficiency and improved fabrication tolerance [91,92]. To design a metalens with an NA of 0.99, metagratings were substituted in the outer region of the metalens [93]. The bending angle of the light was determined by the period of the supercell, and optimization of the metagrating was achieved by adjusting the number and parameters of the elements. The entire lens area was functional, as demonstrated by the collection of light from a sub-diffractive scatterer located at the focus (Fig. 2C). Moreover, a polarization-insensitive metalens with an NA of 1.48 was demonstrated by combining two approaches: oil immersion and metagratings (Fig. 2D) [94]. The focusing efficiencies of these two lenses were approximately 10 % and 42 %; however, these values could be increased by optimizing the metagrating structures. High-efficiency supercells for large deflection angles can be realized through adjoint-based topological optimization [95], and these structures could be generated cost-effectively by using generative adversarial networks [96].

High-NA lenses play a vital role in high-resolution imaging systems, confocal microscopes, lithography, and optical trapping. For imaging applications, metalenses with NAs of 0.8 [31], 0.85 [30], and 1.48 [73] have been successfully demonstrated. In addition, confocal imaging applications have benefited from metalenses with NAs of 0.99 [93], 1.1 [85] and 1.48 [94]. Furthermore, recent advancements in fabrication technology have sparked growing interest in metalens-integrated systems. For example, a patterned metalens on the facet of a functionalized optical fiber was demonstrated, achieving an NA of 0.88 with diffraction-limited performance. This advancement enables optical trapping of microbeads and *E. coli* bacteria (Fig. 2E) [97]. Additionally, a metasurface with an NA of 1.2 was demonstrated for on-chip trapping, exhibiting trap stiffness comparable with that of a conventional objective lens [99]. Moreover, a metalens with an NA of 0.85, integrated at the tip of a single-mode fiber for direct laser lithography, achieved a remarkable width of written lines of 220 nm (Fig. 2F) [98].

3.1.2. Wide field-of-view

Field-of-view (FOV) is another critical metric of lens performance. An imaging device with a wide-FOV can visually capture the surrounding scene in a single frame [100]. Wide-FOV imaging is used extensively in various fields, including photography, microscopy, and light detection and ranging (LiDAR). At normal incidence, an aberration-free metalens could be realized by using the hyperbolic phase profile and sufficient meta-atom sampling [101]. However, at large angles of incidence (AOIs), off-axis aberrations, such as coma, astigmatism, and field curvature, are more pronounced and hinder wave convergence at the focal point [102].

An ideal phase profile that is derived from Fermat's principle can be expressed as follows [103]:

$$\phi(x,\theta) = -\frac{2\pi}{\lambda}\left[x\sin\theta + \sqrt{f^2 + (x - x_0(\theta))^2} - \sqrt{f^2 + x_0(\theta)^2}\right], \tag{3}$$

where θ is the angle of incidence and $x_0(\theta)$ indicates the focal location. eq. (3) is evidently angle-dependent and cannot be realized unless all the meta-atoms exhibit perfect angle-dispersive properties that satisfy this ideal phase. A deviation between the ideal and hyperbolic phases leads to off-axis aberrations. Traditional metalenses, which are based on the hyperbolic phase profile, often have a restricted FOV due to the typical neglect of angular dispersion of phase [101]. Therefore, minimizing off-axis aberrations with a singlet metalens, particularly for a high-NA, proves challenging. The limited FOV can be understood from a Fourier transform analysis of the field distribution [104]. Only k-vector components within the range of $[-k_0,\ k_0]$ contribute to focusing, while components outside this range become evanescent and do not contribute to the focusing process. As discussed, achieving a wide-FOV is particularly challenging for high-NA systems because enlarging the NA increases the magnitude of the high-k components [105]. For more details, readers can refer to Refs. [100,104,105]. One method for reducing off-axis aberrations involves the use of a singlet metalens with a solid substrate aperture stop, so-called Chevalier landscape metalens [106,107]. The incident waves, whether normal or oblique, are effectively controlled by the aperture stop positioned at the front focal plane of the metalens. This aperture stop enhances wave focusing efficiently, resulting in improved angular response while minimizing aberrations. This approach was employed to realize a flat fisheye lens with a near-180°-FOV in the mid-infrared (MIR) range [107]. Fig. 3A shows a schematic of a wide-FOV metalens, which achieves a focusing efficiency of approximately 40 % for all AOIs ranging from 0° to 85°. In another study, a catenary optics-based wide-FOV metalens was developed through isophase streamline optimization, eliminating unwanted diffraction orders in the infrared range for diverse angles [108]. It featured diffraction-limited imaging over a wide-FOV up to 178° with an aperture stop in the silicon-on-sapphire substrate (Fig. 3B). Additionally, a Huygens metalens based on this approach was developed to create a compact wide-angle outdoor NIR camera with an approximate FOV of 30° [106].

Interestingly, an alternative approach to make singlet wide-FOV

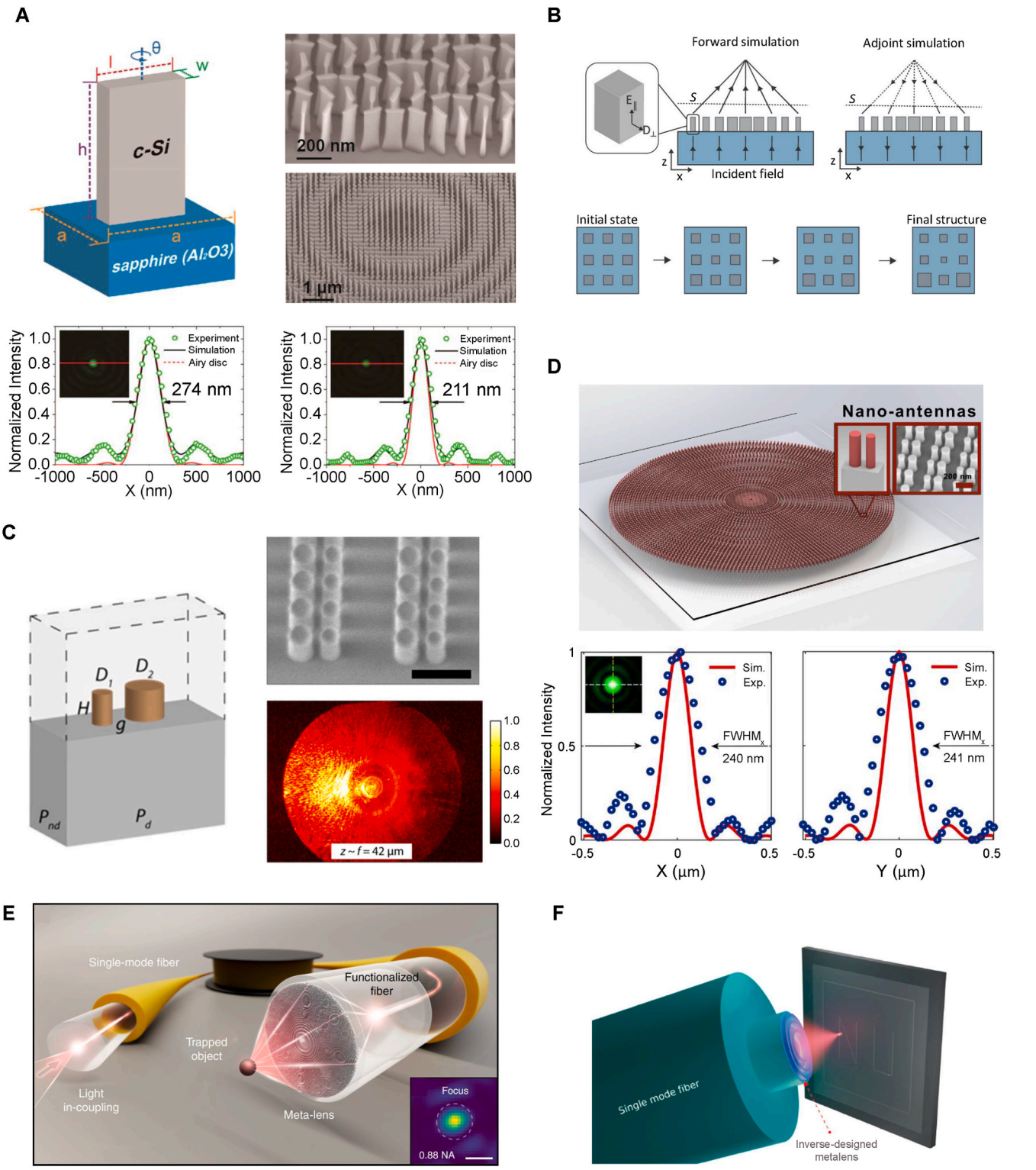

Fig. 2. Ultra-high-NA optical metalenses. (A) Illustration of c-Si nanobricks and SEM images of the fabricated metalens. The meta-atoms optimized for length, width, height, and center-to-center spacing. The FWHM of the focal spot is 274 nm (in air) and 211 nm (in oil). Reproduced with permission from [73]. Copyright 2018 American Chemical Society. (B) Schematic of the adjoint optimization process. Reproduced with permission from [89]. Copyright 2021 American Chemical Society. (C) Schematic of the asymmetric nanoantennas and SEM images of the tilted views of 82° bent nanoantennas (scale bar: 500 nm). Reproduced with permission from [93]. Copyright 2018 American Chemical Society. (D) Schematic of an ultra-high-NA metalens combining two approaches; oil immersion and asymmetric nano-antennas. The FWHM of the focal spot is 240 nm (horizontal) and 241 nm (vertical) for unpolarized light. Reproduced with permission from [94]. Copyright 2022 Wiley-VCH. (E) Schematic of the ultra-high-NA meta-fiber system for optical trapping. Reproduced with permission from [97]. Copyright 2021 Springer Nature. (F) Schematic of the fiber tip metalens on the single-mode fiber for direct laser lithography. Reproduced with permission from [98]. Copyright 2021 American Chemical Society.

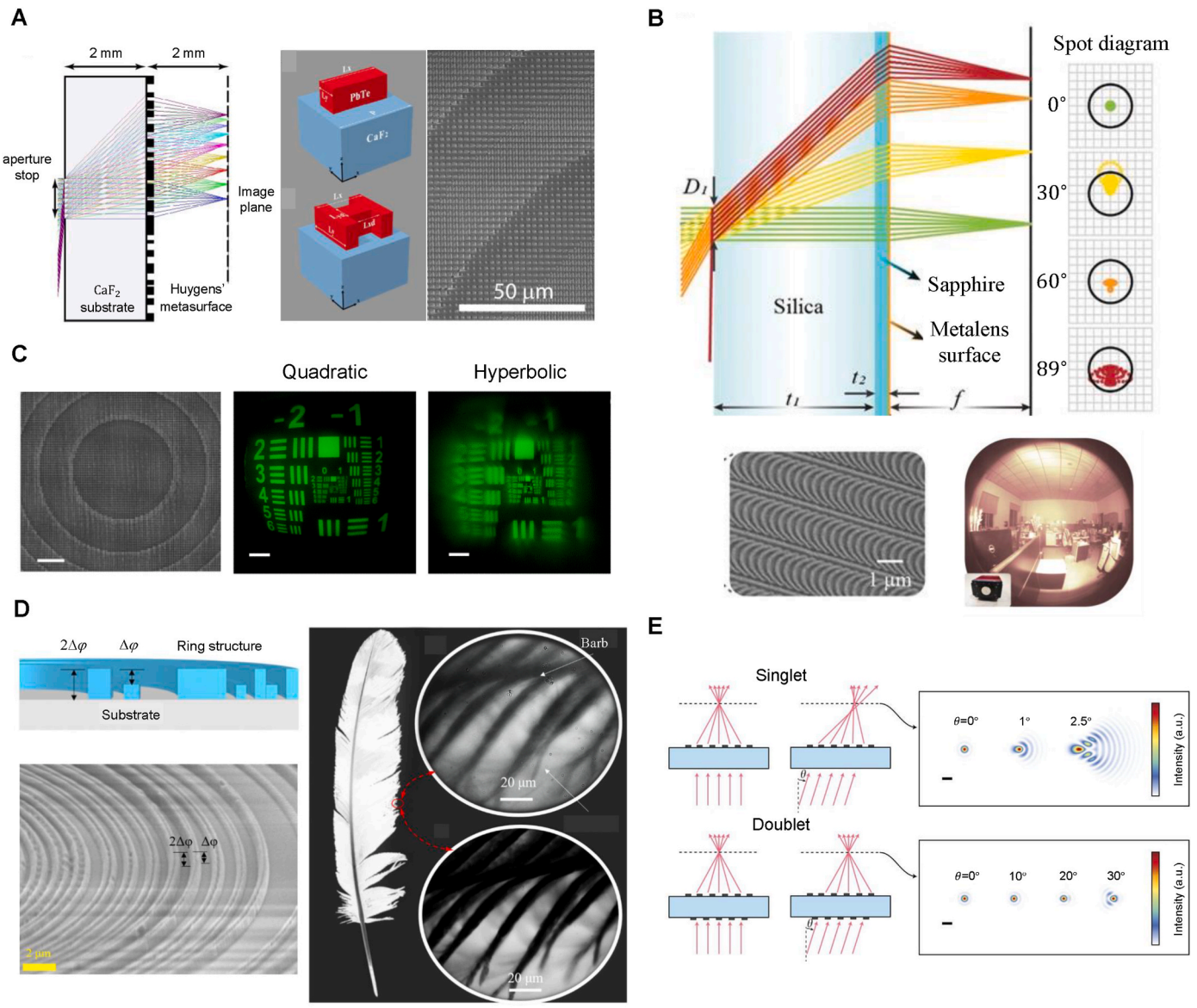

Fig. 3. Wide-FOV metalenses. (A) Side view of the Chevalier landscape metalens. The metalens comprises Huygens meta-atoms. Reproduced with permission from [107]. Copyright 2020 American Chemical Society. (B) Side view of the catenary optics-based wide-FOV metalens with an aperture stop, and the SEM image of fabricated metalens and realized ultr wide-FOV imaging. Reproduced with permission from [108]. Copyright 2021 Wiley-VCH. (C) The SEM image of the single-layer quadratic metasurface (scale bar: 3 μm). and imaging test results of the quadratic- and hyperbolic-phase metalens with a USAF 1964 chart (scale bar: 100 μm). Reproduced with permission from [109]. Copyright 2020 American Chemical Society. (D) Cross-sectional and SEM image of the 32°-FOV single-layer metalens, microscopic imaging of the metalens (up), and 20 × Zeiss objective (down). Reproduced with permission from [110]. Copyright 2020 Wiley-VCH. (E) Schematic of light focusing by singlet and doublet metalenses. Near-30°-FOV is realized by reducing off-axis aberrations with the doublet metalens. Reproduced with permission from [111]. Copyright 2016 Springer Nature.

metalenses is to employ a quadratic phase profile, in contrast to the conventional hyperbolic phase profile. The quadratic phase profile, which was proposed in 2017, allows perfect transformation from rotational to translational symmetry [112]. It can be expressed as follows:

$$\phi(r,\theta) = -\frac{k_0}{2f}r^2 - k_0 x\sin\theta = -\frac{k_0}{2f}\left[(x+f\sin\theta)^2 + y^2\right] + \frac{fk_0}{2}\sin^2\theta. \quad (4)$$

The last term on the right-hand side in eq. (4) can be ignored because it is independent of *r*. There is only a translational shift of the focal position with respect to the AOIs. Considering this, the rotational effect of oblique incidence waves is perfectly converted into the translational symmetry of the focusing beam along the focal plane. Fig. 3C depicts a single-layer metalens designed with a quadratic phase profile. The full width at half maximum (FWHM) of its focal spot remains consistent up to 89°, enabling it to surpass existing metalenses in terms of imaging quality and wide-angle capabilities [109]. Several studies have also utilized the quadratic phase for various applications, including fingerprint detection [113], retroreflector [114], bi-functional imaging [115], and spin-decoupled vortex recognition [116].

Moreover, the creation of a single-layer wide-FOV metalens is feasible without relying on the quadratic phase profile. For example, a 32° FOV single-layer metalens was achieved using the epsilon-greedy algorithm to optimize two sets of concentric nanoring structures with varying heights [110]. The imaging performance of this metalens was comparable with that of a commercial lens (Fig. 3D).

Utilizing the doublet configuration, which involves embedding two metasurfaces on either side of a substrate, is another method for achieving a wide-FOV. The hyperbolic phase profile effectively corrects

spherical aberrations under normal incidence but introduces coma aberrations for oblique incidence. Conversely, the quadratic phase profile is capable of effectively reducing off-axis aberrations while inherently exhibiting spherical aberration. However, doublet metalenses can be designed to simultaneously reduce both spherical and off-axis aberrations [104,111,117,118]. In 2016, a monochromatic doublet metalens with a FOV of 60° was demonstrated [111]. Fig. 3E presents a direct comparison of the focusing performance between singlet and doublet metalenses. In 2017, a metalens doublet was introduced, which comprised of two metalenses: an aperture metalens serving as the Schmidt plate for phase correction and a focusing metalens functioning as the spherical lens [117]. The designed metalens had an NA of 0.44 and a FOV of 50°, and it demonstrated diffraction-limited monochromatic focusing performance. Recently, a comprehensive analysis of design methods and fundamental limitations was conducted [119], which highlighted the constraints in optimization-based doublet metalens design. Besides single-wavelength applications, various studies have explored the potential for developing doublet achromatic wide-angle metalenses [120–122]. Doublet metalenses can also be designed to have different functionalities, such as wide-angle sub-diffraction focusing [123], focal adjustable system [124], and endoscopy system [125].

3.1.3. Achromatic focusing

Material dispersion leads to variations in focal points, which can degrade image quality and focusing efficiency, particularly in multi-wavelength or broadband scenarios. Therefore, the correction of chromatic aberration is essential. In conventional optical lenses, this aberration is typically corrected by combining multiple optical components, resulting in a complex and bulky optical system. Chromatic aberration also appears in metalenses owing to the dispersion characteristics of meta-atoms. One strategy for achieving a broadband achromatic metalens involves introducing a wavelength-dependent reference phase $C(\lambda)$ to compensate for the phase variations at different wavelengths. The corresponding phase profile can be expressed as [126]

$$\phi(x,y,\lambda) = C(\lambda) - \frac{2\pi}{\lambda}\left(\sqrt{x^2+y^2+f^2} - f\right). \tag{5}$$

A reflective broadband achromatic metalens (1200–1680 nm) [127] and its transmissive counterpart (400–660 nm) [128] were demonstrated using a linear reference phase inversely proportional to the wavelength, defined as $C(\lambda) = \alpha/\lambda + \beta$. Here, $\alpha = \chi\frac{\lambda_{\max}\lambda_{\min}}{\lambda_{\max}-\lambda_{\min}}$ and $\beta = -\chi\frac{\lambda_{\min}}{\lambda_{\max}-\lambda_{\min}}$, where $\lambda_{\min}$ and $\lambda_{\max}$ represent the lower and upper limits of wavelength, and χ is the largest additional phase shift. In this scenario, the achromatic phase profile can be divided into two terms: the wavelength-independent phase $\phi(x,y,\lambda_{\max}) = -\frac{2\pi}{\lambda_{\max}}(\sqrt{x^2+y^2+f^2}-f)$ and the wavelength-dependent phase $\Delta\phi'(x, y, \lambda) = -2\pi\left(\sqrt{x^2+y^2+f^2}-f\right)(1/\lambda - 1/\lambda_{\max}) + C(\lambda)$. The former term was realized using the geometry phase approach and the latter term was obtained from the integrated-resonant states of coupled nanostructures. In the development of the broadband achromatic metalens, Sajan et al. [72] mathematically derived the fundamental limits of the trade-offs among the lens diameter, NA, and operational bandwidth as follows:

$$\Delta\omega \le \frac{c\Delta\phi'}{R_{\max}\left(\frac{1}{\mathrm{NA}} - \sqrt{\frac{1}{\mathrm{NA}^2}-1}\right)}, \quad \Delta\phi' = \left(\frac{d\phi}{d\omega_{\max}} - \frac{d\phi}{d\omega_{\min}}\right)\Delta\omega, \tag{6}$$

where c is the speed of light, ω is the angular frequency, $\Delta\omega$ is the operational bandwidth, and $R_{\max}$ is the maximum radius of the lens. The term $\frac{d\phi}{d\omega}$ denotes the dispersion of eq. (5), which can be reformulated as $\phi(r,\omega) = \phi_0(r) + \frac{d\phi(r)}{d\omega}(\omega - \omega_0)$, with $\phi_0(r)$ representing the phase at a reference frequency ω_0. $\frac{d\phi}{d\omega}|_{\max}$ and $\frac{d\phi}{d\omega}|_{\min}$ correspond to the dispersion at the edge and center of the lens, respectively, with a choice of the reference phase $C(\omega) = \frac{\omega}{c}\sqrt{r_0^2+f^2} + C_0$, where r_0 is the radius of the lens and C_0 is the constant phase. By considering this aspect, a broadband achromatic metalens that approaches this limitation was designed and fabricated (lens diameter: 100 μm, NA: ~0.24, operational bandwidth: 1300–1650 nm). The meta-atoms are designed to be rotationally symmetric with sufficient height to exhibit polarization-insensitivity and a wide range of phase and dispersion coverage (Fig. 4A).

Another alternative approach is to compensate for group delay and group delay dispersion. The Taylor expansion of the phase profile $\phi(r,\omega)$ near the target wavelength ω_d can be expressed as [129]

$$\phi(r,\omega) = \phi(r,\omega_d) + (\omega-\omega_d)\frac{\partial\phi(r,\omega)}{\partial\omega}_{\omega=\omega_d} + (\omega-\omega_d)^2\frac{\partial^2\phi(r,\omega)}{2\partial\omega^2}_{\omega=\omega_d} + \cdots, \tag{7}$$

where the terms indicate the phase, group delay, and group delay dispersion, respectively, in sequential order. Typically, conventional dispersive metalenses are designed without considering higher-order terms such as group delay and group delay dispersion, leading to chromatic aberration. However, when these terms are considered, it is feasible to obtain a broadband achromatic metalens. In Ref. [129], a broadband achromatic metalens was realized by compensating these terms using single and multiple TiO_2 nanofin elements. The researchers designed a broadband achromatic metalens with an NA of 0.2 and a focal length of 63 μm for light with wavelengths ranging from 470–670 nm. Fig. 4B shows the required group delay and group delay dispersion for such a metalens. It exhibited achromatic focusing with an efficiency of 20 % at 500 nm. Additionally, full-color imaging was demonstrated capability with a broadband achromatic metalens having an NA of 0.02 and a diameter of 220 μm. As discussed, the dielectric nanopillars can be considered truncated waveguides, and the corresponding phase retardation is $\phi = \frac{\omega}{c}n_{\mathrm{eff}}h$, where h is the height of the meta-atom. Thus, the dispersion of this meta-atom is $\frac{\partial\phi}{\partial\omega} = \frac{1}{c}n_{\mathrm{eff}}h + \frac{\omega}{c}\frac{\partial n_{\mathrm{eff}}}{\partial\omega}h$. Here, the use of meta-atoms with elongated structures and materials with higher refractive indicies allows the realization of broadband achromatic metalenses with larger diameters, higher NAs, and larger operational bandwidths. However, owing to the limitations of the fabrication and natural materials, discrete RGB metalenses are emerging as an alternative for practical applications.

One strategy for designing achromatic metalenses involves the spatial-multiplexing and spatial-interleaving methods [135,130]. The spatial-multiplexing method divides the aperture into multiple zones, each assigned a corresponding lens profile. Meanwhile, the spatial-interleaving method interleaves meta-atom configurations within an aperture. Fig. 4C shows a schematic of an achromatic RGB metalens designed using the spatial-interleaving method (NA: 0.87, diameter: 450 μm) [130]. Despite its straightforward design strategy, unwanted interference between meta-atoms may result in ghost imaging and virtual focus.

Another method is stacking multiple layers of metasurfaces [131,136,137]. For example, in one study, an RGB achromatic doublet metalens was demonstrated [131]. This metalens had an NA of 0.8 and a diameter of 1 mm, with the reference phase optimized by utilizing an additional degree of freedom in the vertical layer within the stack. The inter-layer distance was less than three times the wavelength, and it achieved simultaneous focusing of all three wavelengths (Fig. 4D). Moreover, broadband achromatic metalenses were realized by merging the phase plate and metalens layer [132]. The phase plate and metalens layer were designed using recursive ray-tracing algorithms and phase libraries. Metalenses with entrance pupil diameters of 20, 40, 80 μm and NAs of 0.27, 0.11, and 0.06 were fabricated, exhibiting diffraction-limited focusing with an average efficiency of over 60 % across a broad bandwidth spanning 1000–1800 nm (Fig. 4E).

Furthermore, inverse design could be a promising strategy for

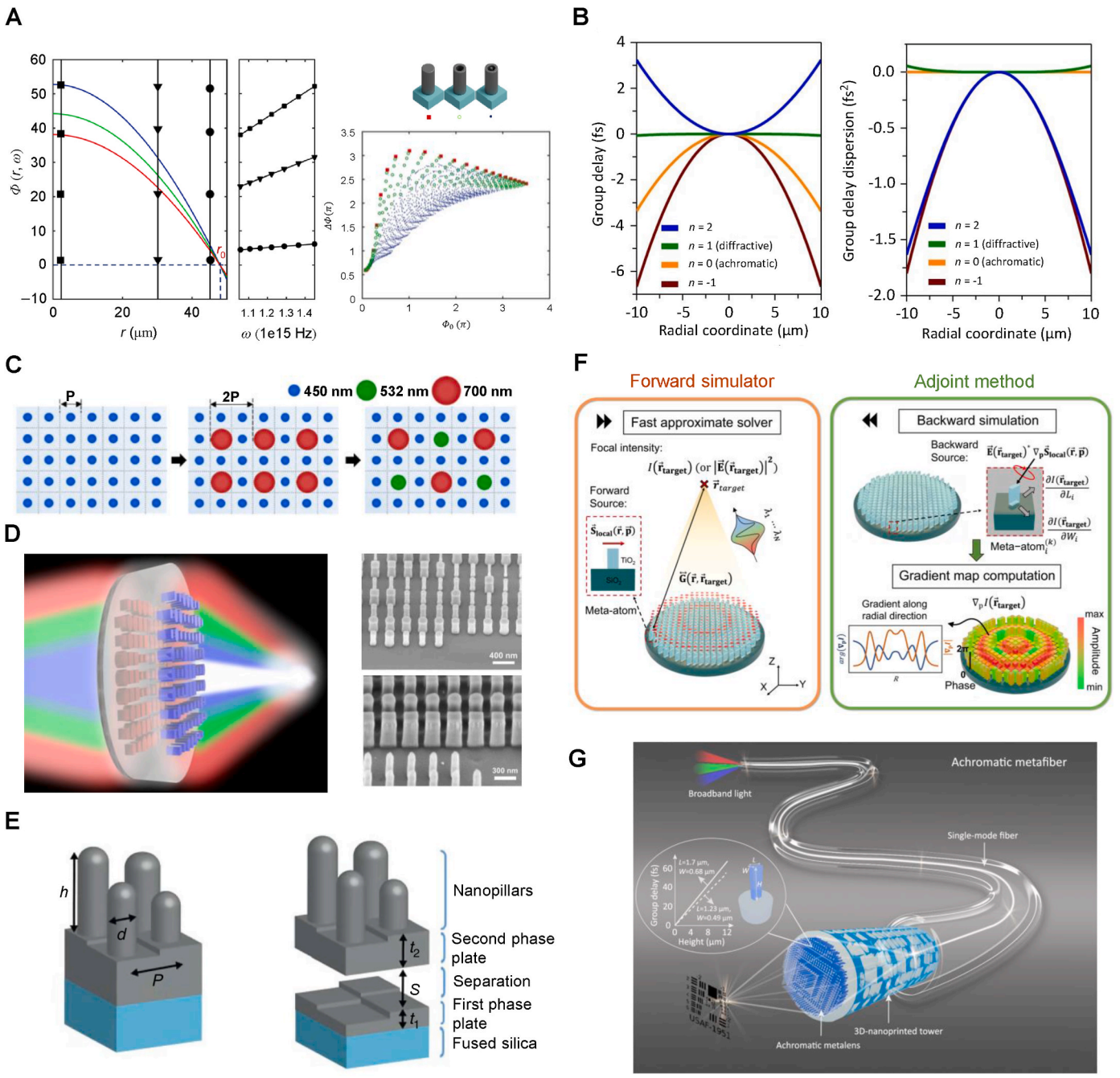

Fig. 4. Achromatic metalenses. (A) Spatial and spectral phase profiles for a broadband achromatic metalens and the calculated phase and dispersion of meta-atoms. Reproduced with permission from [72]. Copyright 2018 Springer Nature. (B) Required group delay and group delay dispersion for achromatic metalens (orange line). Reproduced with permission from [129]. Copyright 2018 Springer Nature. (C) Schematic of the spatial-interleaving method for the achromatic metalens. Reproduced with permission from [130]. Copyright 2022 Optica Publishing Group. (D) Schematic of the RGB achromatic metalens doublet, and SEM image of the c-Si layer (up) and the Si_3N_4 layer (down). Reproduced with permission from [131]. Copyright 2022 American Chemical Society. (E) Unit-cell of the merged phase plate and metalens layer. Introduction of an air gap between the two layers enables the achievement of a higher NA and larger diameter. Reproduced with permission from [132]. Copyright 2020 Springer Nature. (F) Schematic of forward simulator and adjoint method for designing a large scale achromatic metalens. Reproduced with permission from [133]. Copyright 2022 Springer Nature. (G) Schematic of a metalens-integrated achromatic meta-fiber system. Reproduced with permission from [134]. Copyright 2022 Springer Nature. (For interpretation of the references to color in this figure legend, the reader is referred to the Web version of this article.)

designing achromatic metalenses. For example, a high-NA and broadband achromatic metalens was designed through adjoint-based topology optimization (NA: 0.9, operational bandwidth: 450–700 nm) [138]. In a separate study, a large-area RGB achromatic metalens, featuring a diameter of 1 cm and an NA of 0.3 was successfully created by employing a fast approximate solver and an adjoint method, leading to a substantial reduction in computational expenses while maintaining a focusing efficiency of ~15 % across the RGB spectrum (Fig. 4F) [133].

Achromatic lenses are essential in hyperspectral imaging applications, including fluorescence microscopy [139], bioimaging [140], coherent Raman scattering imaging [141], detection systems [142], light-field camera [143,144], and augmented reality (AR) and virtual reality (VR) devices [133,145,146]. Further details about two prominent imaging applications, light-field camera and AR/VR devices, will

be discussed in the applications section. Moreover, the correction of aberrations is crucial for various optical systems. In fiber optics, for example, correcting chromatic aberration is critical for realizing long-range communications and fiber imaging. To address this issue, an achromatic meta-fiber was proposed [134]. By patterning a metalens on the hollow tower printed on the flat end of a single-mode fiber, it focuses light, exhibiting a broad bandwidth of 1250–1650 nm and polarization-insensitive properties (Fig. 4G).

3.2. Acoustic perspective

3.2.1. High numerical aperture

Achieving high-NA, which has been mainly discussed in the optical field, can also play a key role in the acoustic domain. For instance, high-NA metalenses possess the capability to enhance focusing efficiency and improve imaging resolutions in acoustics. This, in turn, facilitates the precise detection of internal defects and material damage, consequently elevating the accuracy and reliability of non-destructive testing. Moreover, within the domain of medical imaging, high-NA acoustic metalenses can enhance the resolution of ultrasound. Furthermore, in applications such as high-intensity focused ultrasound (HIFU), high-NA acoustic metalenses enable the confinement of sound-matter interactions to smaller volumes, thereby enhancing targeting accuracy and efficiency with high intensities. Consequently, this ability has the potential to minimize damage to surrounding biological tissues [147].

As previously discussed, conventional metalenses rely on local phase modulation, a process highly dependent on the discretization level of meta-atoms. Achieving a high-NA requires a very dense array of small-period meta-atoms. However, it is difficult to scale down complex structures, such as zig-zag structures. Moreover, local phase modulation-based high-NA metalenses are affected by higher-order effects due to the impedance mismatch between the incident and scattered fields [148], resulting in low focusing efficiency. To address these limitations, the metagrating method, introduced as an alternative approach, has been proposed to realize a high-NA acoustic platform with the help of the nonlocality. For example, a high-NA ultrasonic metagrating lens was proposed [149]. Multilayered stepped meta-atoms, as illustrated in Fig. 5A, were used to achieve an NA of 0.94 (numerically) and 0.74 (experimentally). The basic mechanism of the proposed metagrating is to create an uneven reflected pressure distribution with high diffraction orders. To realize complex design, a semi-analytical approach was used to optimize 26 metargratings, and 22.9 times intensity enhancement and FWHM of 0.6 λ were obtained experimentally (Fig. 5A).

High-NA metalenses also hold promise for wave-energy harvesting. For example, Fan et al. [150] proposed a high-NA underwater metalens for achieving acoustic focusing in a continuous water flow. This metalens features flow-permeable characteristics and has two distinct regions: a central area facilitating water flow and a peripheral region utilizing

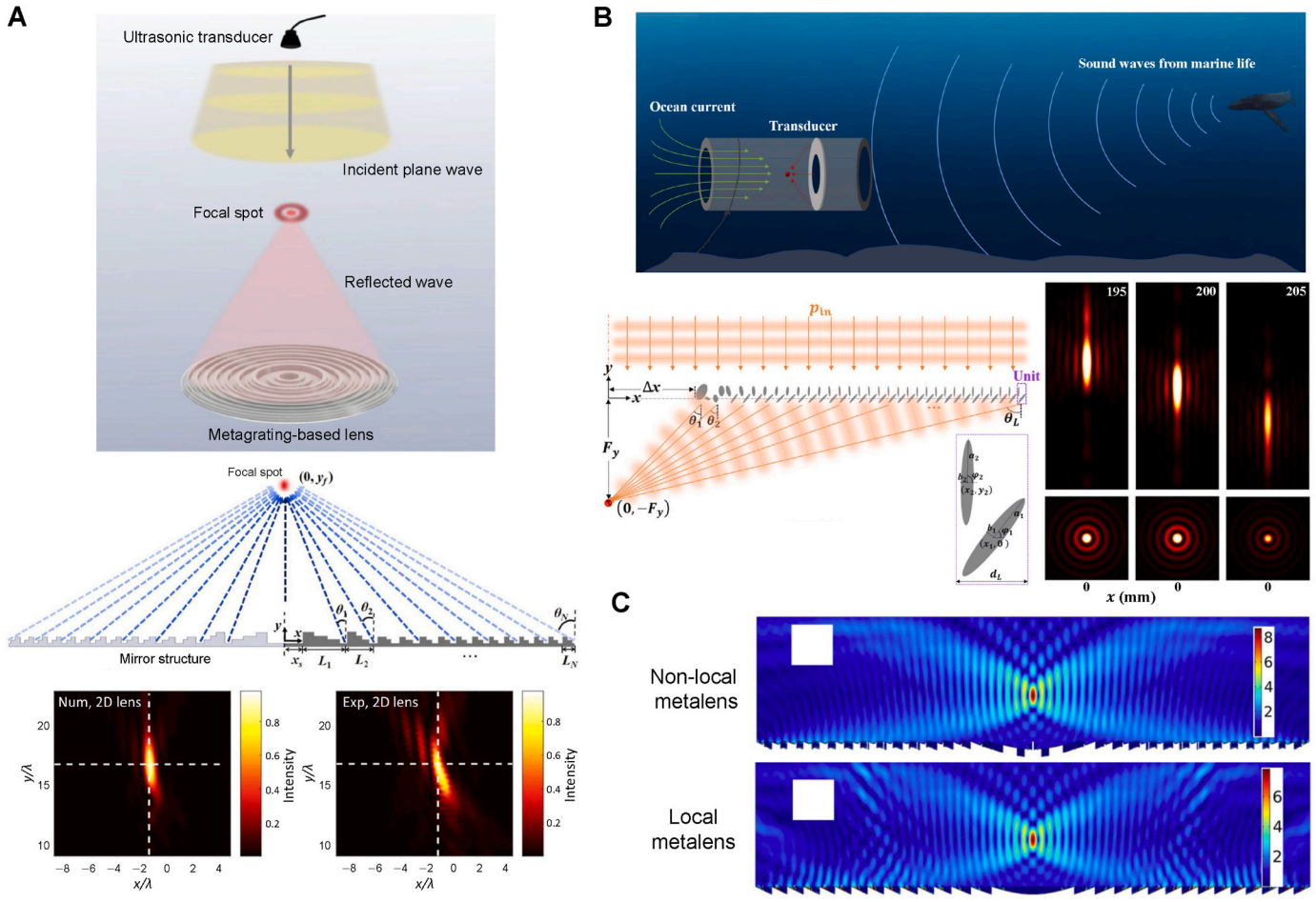

Fig. 5. High-NA acoustic metalenses. (A) Schematic of a high-NA acoustic metalens for reflected ultrasonic wave focusing, and illustration of the metagrating-based design approach. Focusing performance is validated both numerically and experimentally and 0.6 λ of FWHM is measured (10 % lower than the simulated result). Reproduced with permission from [149]. Copyright 2021 American Physical Society. (B) A flow-permeable high-NA acoustic metalens composed of two elliptical iron-cylinder meta-atoms, with sub-diffraction focusing performance obtained under different background flow rates. Reproduced with permission from [150]. Copyright 2023 American Physical Society. (C) Comparison of the focusing intensity field between the non-local high-NA metalens and local high-NA metalens. Reproduced with permission from [151]. Copyright 2023 American Physical Society.

metagratings to focus the incident waves onto the focal point (Fig. 5B). It comprises 32 meta-atoms and was designed using the particle swarm optimization method to control six diffraction orders, thus achieving high focusing efficiency. The NA is 0.952, and the flow-permeable area ratio stands at 26.5 %. Remarkably, despite the substantial flow-permeable area ratio, sub-diffraction focusing was successfully achieved under varying water-flow velocities (Fig. 5B). In another study, Xie et al. introduced a high-NA nonlocal acoustic metalens that incorporated coupling effects, specifically lateral energy exchange along the planar surface [151]. They demonstrated that local metalenses have lower efficiency analytically and proposed a two-step approach to design high-NA nonlocal metalenses: first, obtaining the desired focusing field using an optimization algorithm, and subsequently designing a power flow-conformal structure based on the methodology proposed in Ref. [151]. The nonlocal metalens, characterized by an NA of 0.994 and improved focusing capabilities, was verified through numerical simulations (Fig. 5C).

3.2.2. *Broadband operation*

Acoustic metalenses offer remarkable focusing capabilities in the planar and ultra-thin form factors. However, several notable challenges remain. In comparison with their optical counterparts, acoustic metalenses encounter specific challenges. For instance, achieving achromatic focusing is a primary goal, but it requires ensuring a broad operational range. However, most acoustic metamaterials rely on resonators, which exhibit a limited operational bandwidth due to their highly dispersive responses. Furthermore, consider the visible light spectrum, which covers a relatively narrow range from 400 to 760 nm, spanning less than an octave. By contrast, audible sound encompasses a vast frequency range from 20 Hz to 20 kHz, spanning up to 10 octaves [68]. Consequently, developing a mechanism for broadband sound manipulation is inherently challenging. Thus, various efforts need to be undertaken, aiming to advance the performance and use of acoustic metalenses in real-world applications.

In a recent study, an achromatic acoustic metalens was developed using a bottom-up inverse-design method and dispersion engineering [152]. Through optimization, unit cells featuring counterintuitive designs were designed to manifest either non-dispersive or dispersive properties through adjustments in asymmetric scatterers and zig-zag-like cavities. This metalens exhibited achromatic and broadband focusing capabilities in the frequency range of 1–4 kHz (Fig. 6A). In another study, an easily reconfigurable broadband metalens was developed using a straightforward orifice-based design [153], allowing acoustic focusing over a wide range of frequencies from 3.8 to 10 kHz. However, its functionalities did not include achromatic focusing (Fig. 6B). In addition, a broadband-focusing acoustic metalens, that employed zig-zag channels and operated in the frequency range of 2.5–5.5 kHz was reported [154] (Fig. 6C). The main purpose behind the

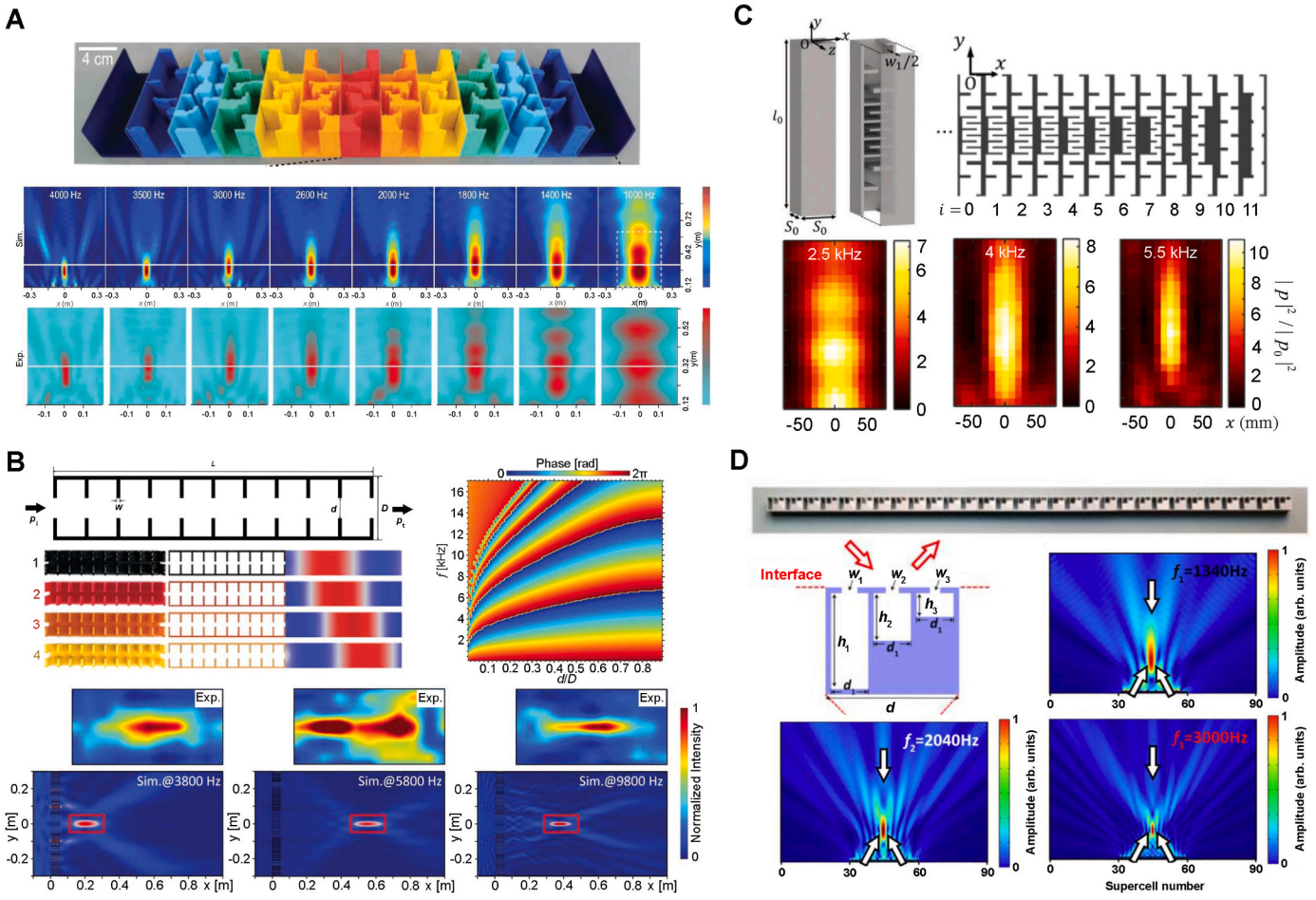

Fig. 6. Broadband acoustic metalenses. (A) Broadband achromatic metalens based on the inverse design affording 1–4 kHz wave focusing. Reproduced with permission from [152]. Copyright 2022 Oxford University Press. (B) Broadband acoustic metalens providing 3.8–10 kHz focusing. Each single unit cell is constructed from a straight waveguide decorated with a series of length-varying slits. Reproduced with permission from [153]. Copyright 2022 Wiley-VCH. (C) Broadband acoustic metalens realized by constructing the impedance-matched unit cells, and 2.5–5.5 kHz acoustic focusing is demonstrated. Reproduced with permission from [154]. Copyright 2022 Elsevier. (D) Multi-frequency achromatic acoustic metalens based on a supercell composed of Helmholtz resonators. Reproduced with permission from [156]. Copyright 2019 American Physical Society.

design of these zig-zag channels was to achieve impedance matching [155], and various factors such as elastic deformation and thermo-viscous losses were also considered in the design. Experimental results demonstrated the occurrence of acoustic focusing within broadband frequencies; however, the disadvantage was that the unit cells were able to cover only a relatively narrow range of effective refractive indices. Furthermore, a reflection-type achromatic metalens was developed using the supercell approach [156]. The supercell comprised different Helmholtz resonators that corresponded to equivalent electronic circuits, resulting in focusing capabilities at multiple frequencies (1.34, 2.04, and 3 kHz) (Fig. 6D). However, bandwidth operation is yet to be achieved. In another study, a broadband acoustic metalens based on cavity-like structures was realized [157], and broadband focusing ranging from 7.56-9.66 kHz was demonstrated both numerically and experimentally.

3.2.3. Others

Last but not least, despite the notable milestones achieved in acoustic metalens technology, efforts are required to realize a wide angular response. The existing acoustic metalenses focus primarily on the normal incidence scenario [158–165], and greater emphasis on exploring uncharted areas is needed to achieve wide-angle focusing capabilities. Just as optical advancements related to wide-FOV have revolutionized the imaging field, the pursuit of analogous strategies in the acoustics domain would contribute to applications such as wide-angle airborne sound collection, sound navigation and ranging (SONAR), acoustic communication, biomedical imaging, diagnostics, and treatments.

4. Tunability and multifunctionality

Despite significant advancements, the main drawbacks of the existing metalenses are their fixed operating bandwidths and functionalities after the device is fabricated [166–169]. Therefore, it is intriguing to explore tunable and multifunctional mechanisms controlled by external stimuli, such as pressure, temperature, humidity, electrical signal, and mechanical deformation [170–174]. In this section, we introduce recent works related to tunable and multifunctional metalenses.

4.1. Tunable and multifunctional optical metalenses

Tunable metalenses, encoded with multiple functions in a single or a few layers, enable selective operation by controlling external electrical, thermal, or mechanical stimuli. Among these methods, the electrical method can be easily and accurately controlled and combined with electrical devices, paving the way for real-time measurements and device integration. We classify optically tunable metalenses according to three tuning mechanisms: (1) controlling the properties of light, (2) reconfigurable metasurfaces, and (3) using active materials.

Tunable metalenses, which depend on the properties of light, such as polarization, wavelength, and orbital angular momentum (OAM), have been employed in various applications. For example, varifocal and multifocal metalenses, whose focal position and length can be arbitrarily adjusted, hold value in capturing 3D information of objects [175], zooming lens [176], and achieving compact polarization imaging [177], chiral imaging [178], and spin-selective imaging system [179]. Integrating liquid crystals (LCs) with a metalens makes it feasible to switch the polarization state of light simply and precisely. For example, one study proposed an electrically controllable bifocal metalens integrated with LCs [176]. This metalens exhibits diffraction-limited focusing with high efficiencies of 43.5 % for left-circular polarization (LCP) and 44 % for right-circular polarization (RCP) and focal lengths of 7.5 and 3.7 mm, respectively (Fig. 7A). Furthermore, it demonstrates remarkable versatility in applications such as sensitive and flexible spectroscopy [180,181] and polarimetry systems [182]. As an intriguing example, a high-resolution spectrometer based on a multi-focal metalens was proposed [181]. This spectrometer was designed to have 180 focal points on the multi-focal ring for working wavelengths of 500–679 nm. It is compact and enables the prominent integration of on-chip photonics integration with 1 nm spectral resolution (Fig. 7B). Additionally, it is possible to implement tunable metalenses that operate in various modes depending on the state of light. In one study, a dual mode metalens encoded by two arbitrary phases, namely the hyperbolic and spiral phases, was proposed [183]. It operated in the bright-field imaging mode for RCP and the edge-enhanced imaging mode for LCP by electrical switching (Fig. 7C). The future direction of tunable metalenses is toward achieving high efficiency and broadband operation while employing a flexible tuning mechanism. However, supporting a variety of functions on just one or a few metasurfaces can lead to crosstalk or unwanted interference between meta-atoms, resulting in low efficiency. Therefore, various algorithms are currently in development to optimize such a design [184].

Reconfigurable metasurfaces provide practical tuning mechanisms that involve adjusting physical dimensions, including the distance between meta-atoms or the relative position of layers. These tunable metasufaces can be adjusted through various mechanical-control methods, including mechanical displacement [185], stretching [186, 191], and rotation [187], which can be incorporated with micro-electromechanical systems (MEMS) or electrical actuators for precise and wide-range modulation. Fig. 7D shows the schematic of a MEMS-integrated doublet metalens system [185]. The effective focal length can be modulated by electrically adjusting the distance between two layers. Fig. 7E shows a stretchable metalens capable of adjusting its focal length through lateral stretching, enabling focal length tuning for RGB wavelengths [186]. A graphene oxide metasurface is printed on a flexible polydimethylsiloxane (PDMS) substrate. When the metalens is uniformly stretched, the period of the graphene oxide ring increases, leading to a change in the phase profile and thereby a longer focal length. The focal length is proportional to the square of the stretch ratio. Fig. 7F shows a Moiré metalens, which can tune the focal length by rotation [187]. The focal length can be tuned over a broad range, from approximately 10-125 mm, and it is inversely proportional to the relative angle of two complementary metasurfaces. This mechanism allows the broad and continuous tuning of the focal length; however, there are challenges to address, such as the alignment of metasurfaces and the duration of the tuning process.

Another method involves composing metasurface with active materials, which exhibit high-contrast responses to various stimuli, such as electrical, thermal, and optical signals. Phase change materials (PCMs), including $Ge_2Sb_2Te_5$ (GST) [192], $Ge_2Sb_2Se_4Te_1$ (GSST) [193], and antimony triselenide (Sb_2Se_3) [188], exhibit distinctive optical properties in their two phases of matter. As an example, a schematic of the tunable metalens based on Sb_2Se_3 is shown in Fig. 7G [188]. The phase of Sb_2Se_3 can be switched using a hotplate or microheater. Despite the distinct phase-based contrast in the optical properties and the tuning speed of PCMs, achieving high efficiency in the UV to NIR region, which is required in practical applications, remains a challenge. Moreover, LCs [189] and graphene [190,194] are promising electrically active materials. In the terahertz region, a tunable chromatic aberration metalens has been proposed [189], featuring a combination of a dielectric metasurface with a photopatterned LCs layer. Each layer is encoded by the resonant and geometric phases, respectively. The metalens operates as a broadband achromatic metalens in the range of 0.9–1.4 THz without an applied bias. When a saturated external bias is applied, it functions as a dispersive metalens by reorienting the LCs perpendicular to the substrates, effectively eliminating geometric phase modulation (Fig. 7H). Another method for a realizing a tunable metalens is to use graphene as illustrated in Fig. 7I [190]. This tunable metalens is composed of a Au film, SiO_2 dielectric layer, single doped graphene layer, and Au nano-antennas. The application of a bias between the graphene layer and Au filmchanges the Fermi energy of graphene, leading to phase modulation. As the Fermi energy varies from 0.1 to 0.9 eV, the focal length shifts from

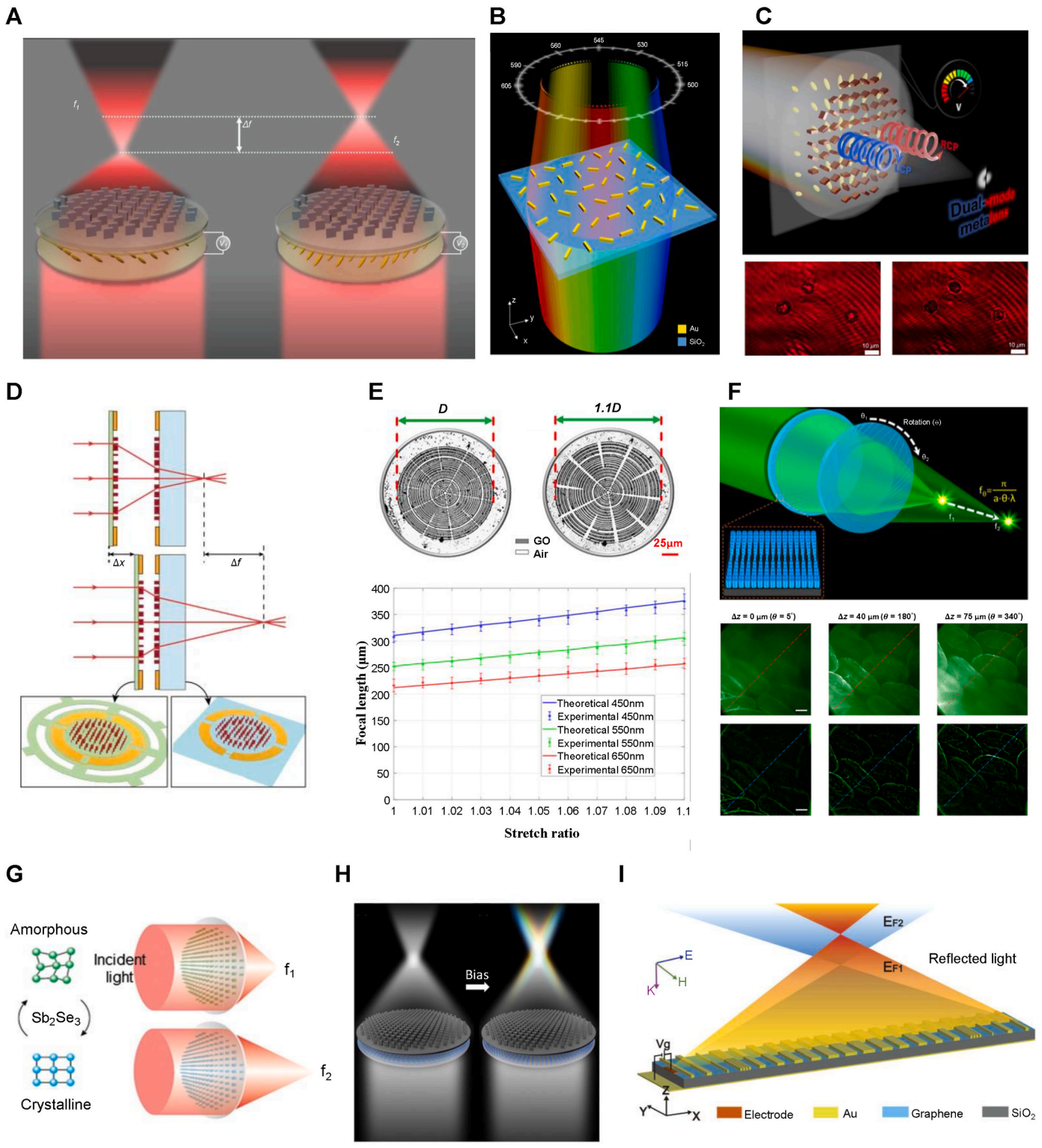

Fig. 7. Tunable and multifunctional optical metalenses. (A) Schematic of an electrically tunable bifocal metalens combined with LCs. Reproduced with permission from [176]. Copyright 2021 Wiley-VCH.(B) Schematic of a multi focal metalens spectrometer. Reproduced with permission from [181]. Copyright 2023 Springer Nature. (C) Schematic of a dual-mode metalens integrated with LCs and bioimaging results (right: bright-field mode, left: edge-enhanced mode). Reproduced with permission from [183]. Copyright 2023 American Chemical Society. (D) Schematic of a MEMS-integrated metalens system. Reproduced with permission from [185]. Copyright 2018 Springer Nature. (E) Bright-field image of an unstretched and stretched graphene metalens, and the focal length according to stretch ratio for RGB. Reproduced with permission from [186]. Copyright 2021 American Chemical Society. (F) Schematic of a varifocal Moiré metalens and fluorescent and HiLo processed images of an intestine tissue samples at three different rotation angles. Reproduced with permission from [187]. Copyright 2021 American Chemical Society. (G) Schematic of a tunable metalens based on PCMs (Sb_2Se_3). Reproduced with permission from [188]. Copyright 2023 Wiley-VCH. (H) Schematic of a tunable metalens based on LCs. Reproduced with permission from [189]. Copyright 2020 SPIE. (I) Schematic of a tunable metalens based on graphene. Reproduced with permission from [190]. Copyright 2020 Optica Publishing Group.

251.5 to 161.1 μm at 10 THz. Moreover, semiconductors [195,196], transparent conducting oxides (TCOs) [197,198] and perovskites [199] are promising candidates for active materials. The use of active materials enables highly flexible metasurface design, and future directions include aspects such as power consumption, response time, efficiency, and flexible tuning systems.

4.2. Tunable and multifunctional acoustic metalenses

The use of mechanical devices may represent a straightforward approach for the tunable control of acoustic waves. For example, the actuators facilitate physical manipulation of cavity volume and length, thereby enabling active modulation of both phase and transmission. By using this strategy, an acoustic metalens that could modulate the reflected phase was realized successfully through the dynamic control of a slider positioned within a Helmholtz resonator to achieve dynamic focal spot transition (Fig. 8A) [200]. Similarly, a tunable acoustic metalens composed of an array of Helmholtz resonators with continuously varying slit widths was developed [201]. Advances in programmable wave manipulation were demonstrated through controlled sound focusing, and other wave manipulation effects, including beam-steering, tweezer-like, and guiding beam generation, were achieved by dynamically adjusting the cavity volume of Helmholtz resonators [202] that modified the water-contained volume using a fluid control system. In addition, an acoustic metalens that modified the channel size of a helical unit cell based on a screw-nut mechanism was introduced [203]. Meanwhile, a piezoelectric multifunctional metasurface powered by a single electrode was developed [204]. This metasurface functioned as a controllable active sound source, combining the benefits of metasurfaces and phased array transducers within a compact form factor. The information related to multifunctionality can be encoded through binary polarization directions on piezoelectric materials—either upward or downward—to facilitate ultrasound imaging and focusing within the MHz frequency range (Fig. 8B). Similarly, a multifunctional bio-inspired metaskin was used to realize ultrasound focusing, vortex formation, and talbot structures for contactless manipulation of living organisms [205]. Furthermore, the introduction of the Janus acoustic metasurface led to the realization of versatile operations, such as acoustic focusing, diffusion, absorption, and beam splitting using unit cells featuring a rotating core, which generated a bias owing to air flow circulation [206]. One of the challenges in enhancing the functionality of metalenses is the coupled modulation of reflected and transmitted waves. To address this challenge, an approach for realizing a transmission-reflected-integrated multifunctional metalens was proposed [207]. Through precise adjustments to the horizontal and vertical matching plates of coated unit cells, decoupled control of both reflected and transmitted waves was achieved, and functionalities similar to a pancratic and multi-focus lens were demonstrated (Fig. 8C).

Recently, a metasurface that generated acoustic vortices exhibiting OAM with spiral phase modulation was proposed [209]. OAM has a helical wavefront, and it has emerged as an innovative approach to improve optical and acoustic information capacities. Further, a multifunctional acoustic metalens rooted in an OAM-based geometric-phase meta-array was introduced [208]. This meta-array utilized pipe-Helmholtz resonator structures to achieve geometric phase modulation [210], leading to the generation of topological charge multiplexed waves and enablement of tunable focusing capabilities (Fig. 8D).

5. Emerging applications

5.1. Applications of optical metalenses

Conventional optical elements tend to be bulky and rigid and lack integrability in optical systems. In this context, metalenses can be a promising alternative in various optical systems owing to their extensive design tools and compatibility with modern fabrication technologies,

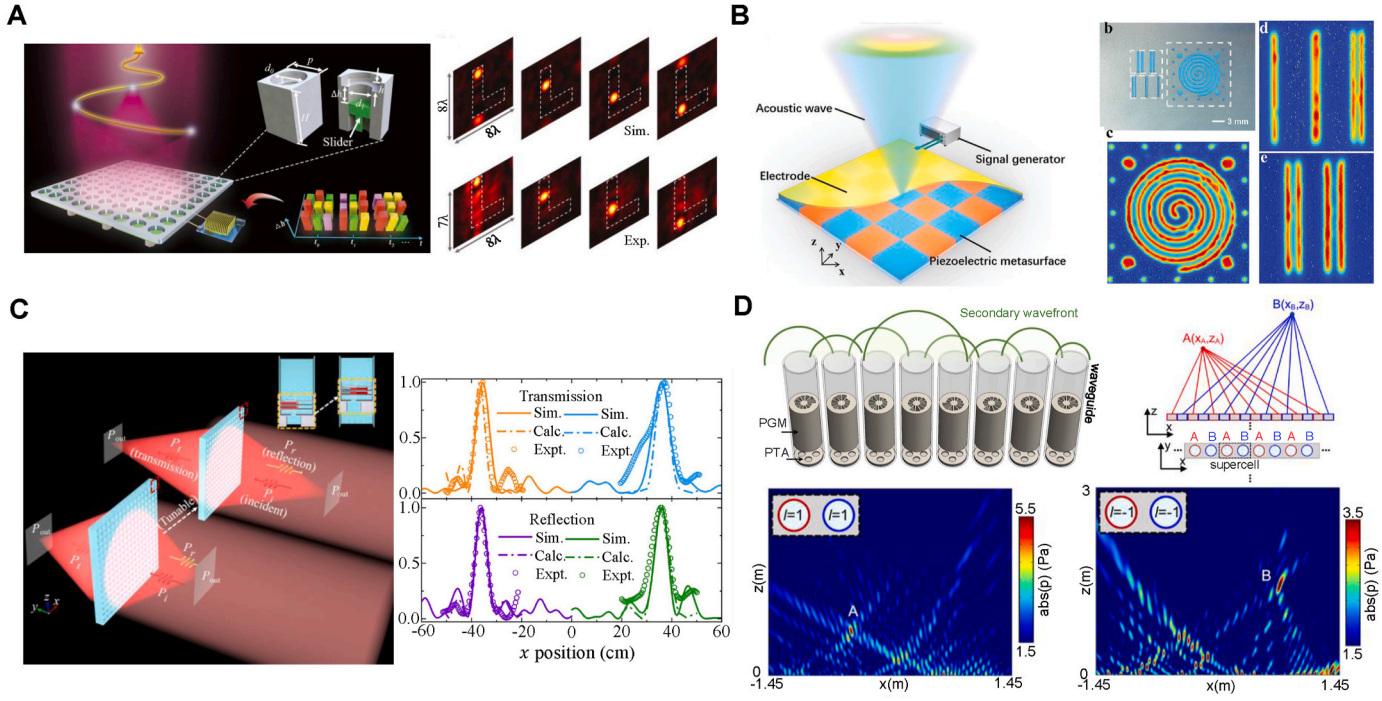

Fig. 8. Tunable and multifunctional acoustic metalenses. (A) Schematic of a tunable metalens for dynamic focal spot tuning by mechanically adjusting the volume of the acoustic cavity. Reproduced with permission from [200]. Copyright 2021 AIP Publishing. (B) Schematic of an active multifunctional metalens driven by coded piezoelectric properties and its ultrasonic imaging functionality. Reproduced with permission from [204]. Copyright 2022 Wiley-VCH. (C) Schematic of transmission-reflection-integrated multifunctional and tunable acoustic metasurfaces and realized pancratic acoustic lensing performance. Reproduced with permission from [207]. Copyright 2022 American Physical Society. (D) Geometric-phase meta array-based multifunctional metalenses. OAM transfer-based phase modulation and multiplexed tunable beam focusing with topological charge are realized. Reproduced with permission from [208]. Copyright 2022 AIP Publishing.

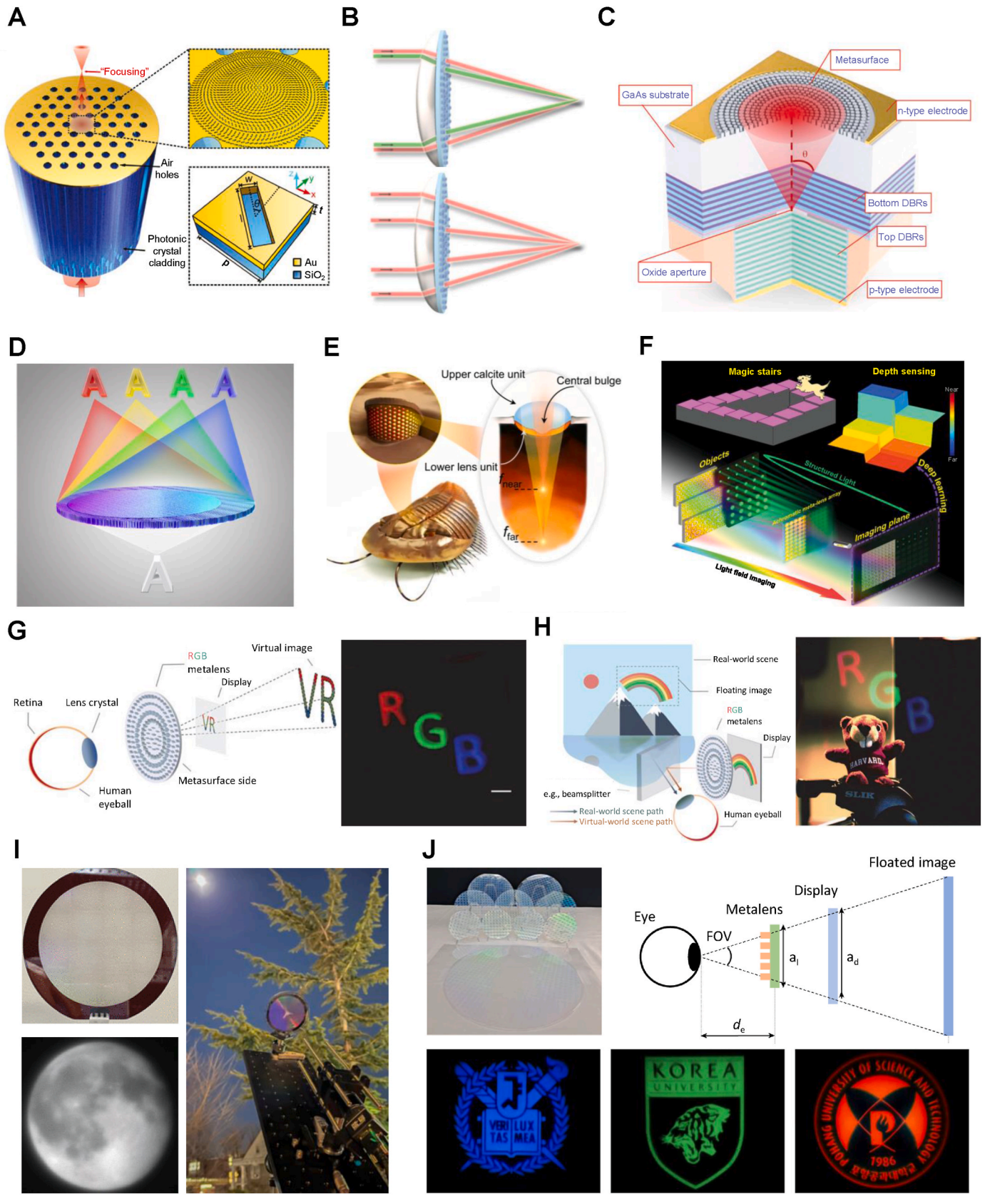

(caption on next page)

Fig. 9. Applications of optical metalenses. (A) Schematic of a metalens-integrated photonic crystal fiber system. Reproduced with permission from [211]. Copyright 2019 De Gruyter. (B) Schematic of metalens-integrated chromatic (up) and spherical (down) aberration-corrected lens. Reproduced with permission from [213]. Copyright 2021 Optica Publishing Group. (C) Schematic of a metasurface-integrated VCSEL. Reproduced with permission from [214]. Copyright 2020 Springer Nature. (D) Schematic of a transversely dispersive metalens for spectral light-field imaging. Reproduced with permission from [216]. Copyright 2022 Springer Nature. (E) Conceptual illustrations of a trilobite-inspired light-field camera. Reproduced with permission from [217]. Copyright 2022 Springer Nature. (F) Schematic of a depth-sensing system; the light-field collection system (bright mode) and the structured light projection system (dark mode). Reproduced with permission from [218]. Copyright 2023 Wiley-VCH. Schematic of (G) VR and (H) AR systems, and imaging results with an achromatic metalens. Reproduced with permission from [146]. Copyright 2021 American Association for the Advancement of Science. (I) An 80-mm-diameter metalens and its application in a telescope system. Reproduced with permission from [219]. Copyright 2023 American Chemical Society. (J) A 1-cm-diameter metalens array on 4″, 6″, 8″, and 12″ wafers and imaging applications. Reproduced with permission from [220]. Copyright 2023 Springer Nature.

exhibiting significant weight reduction and device integration. In modern optics, optical fibers play a crucial role, offering advantages such as low loss, flexibility, and strong light confinement, benefiting applications such as optical trapping, optical communications, and endoscopy. By directly patterning a metasurface on the facet of the fiber, the light in the fiber system can be efficiently manipulated (Fig. 9A) [211]. In photonic integrated circuits, coupling the guided mode and free space mode within the waveguide systems presents a challenging problem. The integration of a metasurface can effectively address this issue by providing flexible coupling of light within the system [212]. Moreover, the aberration of a conventional lens can be corrected by integrating metasurfaces (Fig. 9B) [213]. With design optimization and advanced fabrication technology, a centimeter-scale broadband achromatic metalens can be realized. Metasurfaces can also be integrated with light source systems. For example, a metasurface-integrated vertical cavity surface-emitting laser (VCSEL) was proposed [214]. The metasurface was directly patterned on the backside of the substrate of VCSEL using electron-beam lithography (EBL), and it functioned as a lens for compensating beam divergence. This system exhibits superior beam collimation performance, reducing the beam divergence angle compared to VCSELs without a metasurface (Fig. 9C). Efforts have also been made to manipulate the light emitted by light-emitting diodes (LEDs) [215]. Unlike lasers, the light emitted by LEDs has lower spatial coherence and a broad angular radiation pattern.

3D information of objects can be captured with a light-field camera and reconstructed through a rendering process. Conventional light-field cameras using microlens arrays encounter a significant issue with spherical aberration and restricted depth of field (DOF) due to their large apertures. In 2019, a full color light-field imaging system was demonstrated using a 60 × 60 array of achromatic GaN metalens [143]. The light-field image was captured with this metalens array and reconstructed at different depths using a rendering algorithm. Additionally, a polarization-insensitive broadband achromatic metalens array was developed and demonstrated for the reconstruction of light-field images [144]. Recently, there has been a growing emphasis on the synergy between computational imaging and meta-photonics. In one study, spectral light-field imaging, which includes 3D spatial information with 1D spectral information, was demonstrated using a transversely dispersive metalens array [216]. An impressive spectral resolution of 4 nm and near-diffraction-limited image were obtained by using a spectrum reconstruction algorithm (Fig. 9D). Furthermore, a long DOF light-field camera inspired by trilobites was developed [217]. An array of spin-multiplexed metalenses, each with a different focal length for RCP and LCP light, enabled the capture of a light-field image with a broad DOF while maintaining spatial frequency information. A convolution neural network-based reconstruction algorithm allowed the formation of aberration-corrected images of the scene covering a range of 3 cm to 1.7 km in depth (Fig. 9E). Interestingly, depth sensing for all light levels can also be achieved using an achromatic metalens array [218], which collects the light-field under bright illumination or projects structured light at low light levels. Depth information of objects ranging from 21.0 to 50.5 cm in depth was extracted using neural networks (Fig. 9F).

AR and VR devices demand wide-FOV, full-color, and high-resolution imaging systems. Existing AR and VR devices encounter the challenge of increased device volume due to the use of multi-lens systems for aberration correction [221]. The thin nature of metalenses offers significant advantages in adoption of such systems. A wide-FOV (~90°) AR system was implemented by placing a 20 mm transmissive metalens in front of the eye [222]. This metalens was designed to operate as a transparent glass for co-polarized real-world scenes and as a focusing lens for cross-polarized display images. Chromatic aberration was corrected by placing three dichroic mirrors, which increased the system volume. In recent years, millimeter-to-centimeter-scale achromatic transmissive metalenses have been utilized in AR and VR systems [133,146]. Fig. 9G and Fig. 9H show VR and AR imaging, respectively, with an achromatic metalens [146]. This metalens was designed using constructive interference of light coming from each concentric layer of the dispersion-engineered metalens. For the AR system, the virtual image and real-world scene are blended using an additional optical combiner. The real-world scenes pass through the optical combiner and are projected onto the retina, while the virtual images transmitted through the metalens and deflected by the optical combiner are focused onto the retina.

To realize practical metasurface applications, it is essential to establish fabrication processes that are both cost-effective and scalable. EBL and focused ion beam (FIB) have been used extensively to fabricate μm-scale metalenses due to their high resolution; however, these methods have limitations in terms of time and cost for large-area fabrication. Alternatively, large-area metalenses were fabricated using stepper photolithography [219,223,224] and nanoimprint lithography (NIL) [225,220]. For instance, an 80 mm wafer-scale metalens was fabricated using deep-ultraviolet (DUV) projection stepper photolithography and applied in a telescope system, as depicted in Fig. 9I [219]. Meanwhile, NIL facilitates cost-effective fabrication by transferring the master stamp pattern onto wafers. As depicted in Fig. 9J, arrays of 1-cm-diameter metalenses have been successfully produced using NIL and atomic layer deposition (ALD) processes on wafers, including 4″, 6″, 8″ and 12” [220]. The high-resolution master stamp enables the replication of complex metasurface patterns with a high level of detail. Although stepper photolithography is affected by material and substrate constraints and NIL is influenced by master stamp dependency and operational lifetime, these technologies open up the possibility of practical, real-world metasurface applications.

5.2. Applications of acoustic metalenses

Imaging systems have found significant applications in acoustics, including subwavelength imaging and edge-enhanced imaging facilitated by acoustic metalenses. In 2010, a 2D planar superlens was proposed for subwavelength acoustic imaging, and it exhibited an impressive subwavelength image resolution of 0.07λ [226]. Similarly, a 3D near-field super-resolution imaging metalens was developed to achieve a resolution of 0.02λ by using evanescent wave transmission enhanced by Fabry–Pérot resonance [227]. Additionally, notable progress was made in super-oscillation packets for ultrasonic metalenses [228], and their applications in far-field super-resolution ultrasound imaging (Fig. 10A) and particle manipulation were showcased. In this technique, non-trivial acoustic radiation forces were harnessed using super-oscillation packets. Moreover, the use of acoustic metalenses can

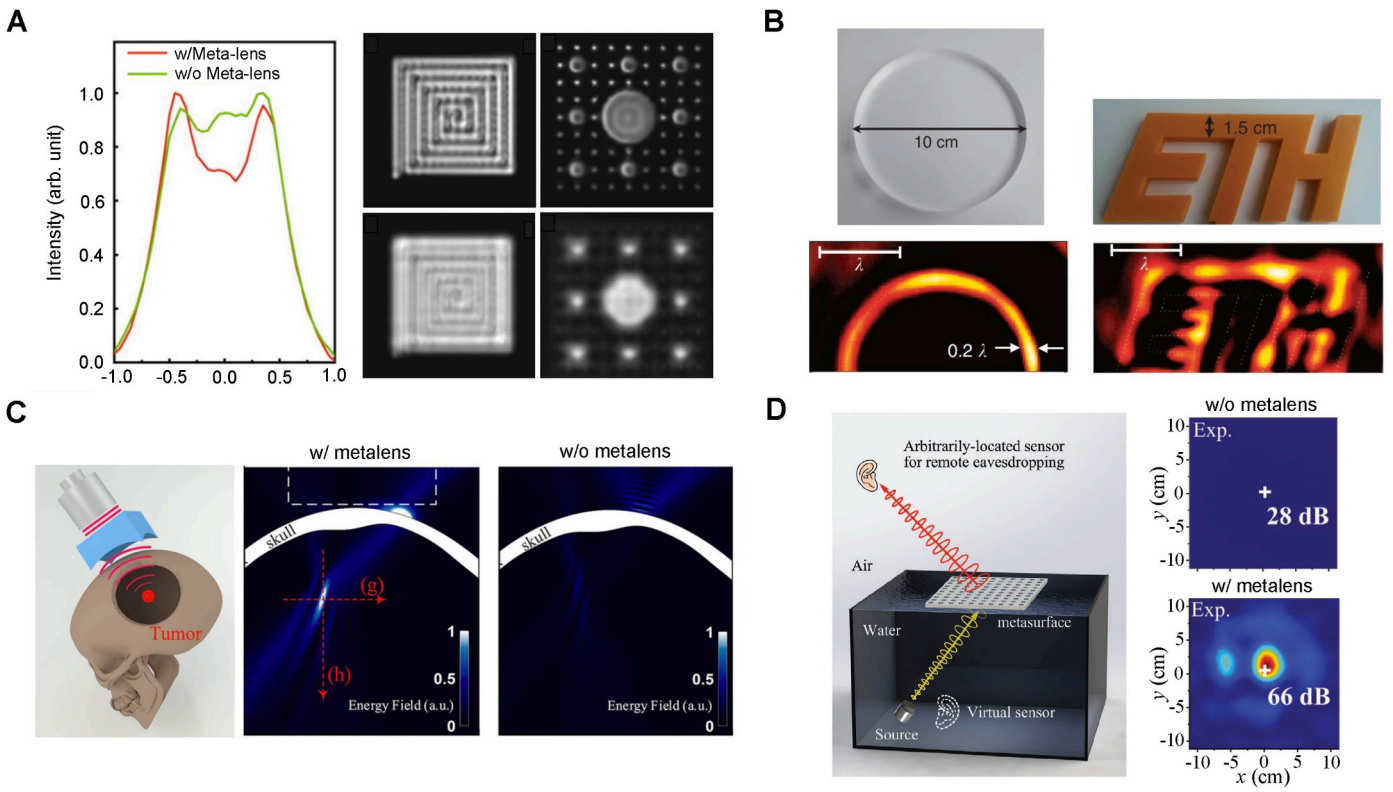

Fig. 10. Applications of acoustic metalenses. (A) Super-oscillation packet-based metalens for superresoution ultrasonic imaging. Reproduced with permission from [228]. Copyright 2019 Springer Nature. (B) Subwavelength-scale edge-detection acoustic metalens by exploiting trapped resonances and experimentally realized edge-enhancement imaging. Reproduced with permission from [236]. Copyright 2015 Springer Nature. (C) Impedance-matched ultrasonic metalens for non-invasive ultrasonic treatment. Reproduced with permission from [238]. Copyright 2022 American Chemical Society. (D) Realization of WTA-focused wave transmission through impedance-matched metalenses. Reproduced with permission from [246]. Copyright 2023 Wiley-VCH.

be extended to bio-imaging. A PC-based ultrasonic metalens was designed for the subwavelength ultrasonic detection of target objects within tissue-like phantoms [229]. Several studies on subwavelength acoustic imaging ranging from audible sound to ultrasound have been conducted [230–232], and a state-of-the-art acoustic metalens with a groundbreaking resolution of less then 0.01λ has been developed [233]. While conventional imaging methods are effective for revealing the structures of objects, edge-enhanced imaging is crucial, particularly in scenarios involving biological tissues that lack distinct natural coloration [234]. This technique, which is beneficial in optical as well as acoustic imaging [235], often requires intricate and time-consuming image-processing algorithms. Moreover, an approach to subwavelength edge-detection was devised using an acoustic metalens (Fig. 10B) [236], which effectively converted evanescent waves into propagating waves by utilizing trapped resonances, resulting in a subwavelength resolution that was approximately five times smaller than the operating wavelength. In addition, a strategy for far-field subwavelength edge-detection was proposed [237]. This strategy relied on spatial frequency filtering and conversion in the near-field, complemented by a spatially symmetric receiving component in the far-field. Acoustic metalenses have versatile applications in focusing and amplifying acoustic energy, and they are particularly advantageous in the ultrasonic domain. Ultrasound serves not only as an imaging tool but also as a therapeutic technique, prominently by leveraging HIFU technology. As discussed, HIFU exploits the thermal effects arising from the absorption of focused ultrasonic energy, thereby providing a robust approach for non-invasive biomedical treatments. Traditionally, non-invasive HIFU treatments for brain tumors have encountered difficulties owing to the substantial acoustic impedance mismatch caused by the skull. The high acoustic impedance of the skull results in near-total reflection at the interface. Recent breakthroughs have emerged with the introduction of complementary metalenses, which are realized through the use of impedance-matching meta-layers [238]. With the incorporation of such metalenses, ultrasound waves can effectively penetrate the cranium with minimal reflection (Fig. 10C). This breakthrough not only facilitates brain treatment [238–240] but also marks a pivotal moment in overcoming the limitations imposed by the acoustic properties of the skull. Acoustic metalenses have proved highly effective in underwater environments, where acoustic waves dominate owing to their low attenuation and scattering properties, which distinguish them from electromagnetic waves [241]. Recent advancements include proposals for acoustic vortex-based communication methods [242,243]. In one study, a multipath acoustic communication platform was introduced for enhancing both information capacity and signal-to-noise ratio (SNR) [244]. By combining spiral and focusing phases, this approach facilitates robust spatial information encoding and decoding with highly concentrated acoustic energy. The transmission of sound waves from water to air (WTA) is challenging owing to the significant acoustic impedance mismatch between these two media. This mismatch induces a pressure release state, allowing the transmission of only ~0.1 % of the acoustic energy [245]. In a recent work, an impedance-matching metalens was proposed to realize WTA eavesdropping [246]. Successful WTA transmissions of tightly focused waves (Fig. 10D) and vortex waves were demonstrated. Similarly, in a study, a hybrid metalens designed using a decoupled inverse design method was employed, and it achieved an ~25.9 dB enhancement in the WTA transmission of focused waves with a center frequency of 10.45 kHz [247]. Additionally, a bio-inspired lotus acoustic metasurface was designed and fabricated for wide-angle WTA transmission [248].

6. Summary and perspective

In this review, we outline the recent strides made in optical and acoustic metalenses. Over the past decade, notable advancements that extend beyond wave focusing to more versatile manipulation of light and sound in the planar form factor have been made. These milestones were achieved through synergies between advanced design strategies and rapidly advancing fabrication techniques.

To date, there has been a notable lack of reviews that bridge the gap between optical and acoustic metalenses. We anticipate that this review will foster a fruitful discussion on the state-of-the-art metalens technology in both wave domains. Given that duality in constitutive parameters can be achieved in controlling each type of wave, the underlying wave physics and resulting wave phenomena share similarities. By highlighting this common thread within a single treatise, we aim to enhance mutual understanding of the principles and methodologies involved in designing metalenses.

In detail, we presented the design challenges involved in the optical and acoustic domains, such as high-NA, wide-FOV, achromatic focusing, and broadband operation. Moreover, we described the development of multifunctionality and tunability to alleviate the constraints of early passive metalenses, enabling wide degrees of freedom. Furthermore, we highlighted emerging applications, such as metalens-integrated systems, 3D imaging and AR/VR devices in the optical domain, and biomedical imaging, therapeutics, and communication in the acoustic domain.

In the field of optics, various exciting applications are possible, including near-eye displays, 3D displays, mobile phone camera lenses, LiDAR sensors for autonomous driving, wearable devices, healthcare, biomedicine, and cutting-edge semiconductor technology. Notably, metalenses have the potential for seamless integration into next-generation electronic devices, including on-chip integrated devices. However, most of these innovations have thus far remained confined to the laboratory or low-volume production phases, requiring further efforts for their transition into real-world commercial applications. To achieve the same, ongoing endeavors encompass advanced fabrication techniques such as cascade domino lithography, two-photon lithography, and grayscale lithography for creating sophisticated metasurfaces. Simultaneously, single-step NIL, photolithography, and roll-to-roll printing have been explored for cost-effective large-scale production. Moreover, employing innovation design strategies through fast solvers and inverse design to optimize devices is promising for enhancing efficiency and expanding their range of functionalities. Notably, in the microwave regime, metalenses fabricated by 3D printing and printed-circuit-board technologies are poised to find applications in 5G networks, wireless communications, and antenna technology, extending their utility beyond the optical regime.

Acoustic metalenses, characterized by their thin and lightweight nature, are well-suited for diverse applications without adding significant bulk or weight to the systems in which they are incorporated. These acoustic metalenses can be tailored for specific frequencies and applications, allowing fine-tuning to meet precise requirements. Notably, they have the potential to enhance the resolution and efficiency of ultrasound systems, offering the promise of more precise medical diagnostics and compact non-invasive treatment systems. These advancements can be particularly beneficial in obstetrics, cardiology, and neurodiagnostics. Furthermore, acoustic metalenses can be useful in structural health monitoring, non-destructive evaluation of the structural integrity of buildings, and assessment of other critical infrastructure. They facilitate the detection of defects and weaknesses with enhanced resolution and reliability. Additionally, acoustic energy harvesting using metalenses presents an exciting avenue for capturing and converting sound energy into electricity. This innovation could provide a sustainable power source for underwater low-energy devices and sensor networks.

Metalens-rooted concepts involving active and multi-purpose metamaterials, artificial intelligence and advanced fabrication techniques will provide promising opportunities by solving the existing challenges that go beyond conventional trends. We hope that driven by ongoing efforts, the development of intriguing applications on the industrial scale will occur rapidly with the use of cutting-edge optical and acoustic metalens technologies.

Author contributions

J.R. conceived the idea and initiated the project. B.O, K·K, and D.L. wrote the manuscript. B.O. and K.K. prepared figures. D.L. and B.O. outlined the manuscript. All authors read and provided feedback on the manuscript. J.R. guided the entire work.

Declaration of competing interest

The authors declare that they have no known competing financial interests or personal relationships that could have appeared to influence the work reported in this paper.

Data availability

Data will be made available on request.

Acknowledgments

This work was financially supported by the POSCO-POSTECH-RIST Convergence Research Center program funded by POSCO, and the National Research Foundation (NRF) grants (NRF-2022M3C1A3081312, NRF-2019R1A2C3003129, NRF-2019R1A5A8080290, RS-2023-00302586, RS-2023-00283667) funded by the Ministry of Science and ICT (MSIT) of the Korean government, and the grant (PES4400) from the endowment project of “Development of smart sensor technology for underwater environment monitoring” funded by Korea Research Institute of Ships & Ocean engineering (KRISO).

References

[1] B. Herman, J.J. Lemasters, Optical Microscopy: Emerging Methods and Applications, 2012.
[2] Y. Xia, G.M. Whitesides, Soft lithography, Annu. Rev. Mater. Sci. 28 (1998) 153–184, https://doi.org/10.1146/annurev.matsci.28.1.153.
[3] H. Kang, et al., Emerging low-cost, large-scale photonic platforms with soft lithography and self-assembly, Photonics Insights 2 (2023) R04, https://doi.org/10.3788/PI.2023.R04.
[4] K. Nakamura, Ultrasonic Transducers: Materials and Design for Sensors, Actuators and Medical Applications, Elsevier, 2012.
[5] S. Lee, et al., A high-fidelity skin-attachable acoustic sensor for realizing auditory electronic skin, Adv. Mater. 34 (2022): 2109545. https://onlinelibrary.wiley.com/doi/abs/10.1002/adma.202109545.
[6] B. Oh, C. Kim, D. Lee, J. Rho, W. Moon, An improved analytic model for designing the polymer-composite stepped-plate transducer using the modified mindlin plate theory, Ultrasonics 131 (2023): 106933. https://www.sciencedirect.com/science/article/pii/S0041624X23000094.
[7] I.F. Akyildiz, D. Pompili, T. Melodia, Underwater acoustic sensor networks: research challenges, Ad Hoc Netw. 3 (2005) 257–279. https://www.sciencedirect.com/science/article/pii/S1570870505000168.
[8] M. Yang, P. Sheng, Sound absorption structures: from porous media to acoustic metamaterials, Annu. Rev. Mater. Res. 47 (2017) 83–114, https://doi.org/10.1146/annurev-matsci-070616-124032.
[9] S. Huang, Y. Li, J. Zhu, D.P. Tsai, Sound-absorbing materials, Phys. Rev. Appl. 20 (2023): 010501. https://link.aps.org/doi/10.1103/PhysRevApplied.20.010501.
[10] D. Lee, et al., Underwater stealth metasurfaces composed of split-orifice–conduit hybrid resonators, J. Appl. Phys. 129 (2021): 105103, https://doi.org/10.1063/5.0042246.
[11] P.A. Deymier, Acoustic Metamaterials and Phononic Crystals, vol. 173, Springer Science & Business Media, 2013.
[12] F.T. Chen, H.G. Craighead, Diffractive lens fabricated with mostly zeroth-order gratings, Opt. Lett. 21 (1996) 177–179. https://opg.optica.org/ol/abstract.cfm?URI=ol-21-3-177.
[13] P. Lalanne, S. Astilean, P. Chavel, E. Cambril, H. Launois, Blazed binary subwavelength gratings with efficiencies larger than those of conventional échelette gratings, Opt. Lett. 23 (1998) 1081–1083. https://opg.optica.org/ol/abstract.cfm?URI=ol-23-14-1081.
[14] D. Fattal, J. Li, Z. Peng, M. Fiorentino, R.G. Beausoleil, Flat dielectric grating reflectors with focusing abilities, Nat. Photonics 4 (2010) 466–470.

[15] W.T. Chen, A.Y. Zhu, F. Capasso, Flat optics with dispersion-engineered metasurfaces, Nat. Rev. Mater. 5 (2020) 604–620.
[16] B. Assouar, et al., Acoustic metasurfaces, Nat. Rev. Mater. 3 (2018) 460–472.
[17] S.-W. Moon, Y. Kim, G. Yoon, J. Rho, Recent progress on ultrathin metalenses for flat optics, iScience 23 (2020): 101877. https://www.sciencedirect.com/science/article/pii/S2589004220310749.
[18] Y. Yang, et al., Integrated metasurfaces for re-envisioning a near-future disruptive optical platform, Light Sci. Appl. 12 (2023) 152.
[19] S. So, et al., Multicolor and 3d holography generated by inverse-designed single-cell metasurfaces, Adv. Mater. 35 (2023): 2208520. https://onlinelibrary.wiley.com/doi/abs/10.1002/adma.202208520.
[20] A. Tittl, et al., Imaging-based molecular barcoding with pixelated dielectric metasurfaces, Science 360 (2018) 1105–1109. https://www.science.org/doi/abs/10.1126/science.aas9768.
[21] A. Silva, et al., Performing mathematical operations with metamaterials, Science 343 (2014) 160–163. https://www.science.org/doi/abs/10.1126/science.1242818.
[22] J. Xu, et al., Acoustic metamaterials-driven transdermal drug delivery for rapid and on-demand management of acute disease, Nat. Commun. 14 (2023) 869.
[23] L. Zhang, et al., A wireless communication scheme based on space-and frequency-division multiplexing using digital metasurfaces, Nature electronics 4 (2021) 218–227.
[24] M. Ossiander, et al., Extreme ultraviolet metalens by vacuum guiding, Science 380 (2023) 59–63. https://www.science.org/doi/abs/10.1126/science.adg6881.
[25] J. Carcione, F. Cavallini, On the acoustic-electromagnetic analogy, Wave Motion 21 (1995) 149–162. https://www.sciencedirect.com/science/article/pii/0165212594000479.
[26] N.J. Wade, Sound and sight: acoustic figures and visual phenomena, Perception 34 (2005) 1275–1290, https://doi.org/10.1068/p5295. PMID: 16309120.
[27] L. Burns, et al., Acoustic versus electromagnetic field theory: scalar, vector, spinor representations and the emergence of acoustic spin, New J. Phys. 22 (2020): 053050.
[28] G. Ma, P. Sheng, Acoustic metamaterials: from local resonances to broad horizons, Sci. Adv. 2 (2016): e1501595. https://www.science.org/doi/abs/10.1126/sciadv.1501595.
[29] D.R. Smith, et al., Electromagnetic parameter retrieval from inhomogeneous metamaterials, Phys. Rev. E 71 (2005) 036617.
[30] M. Khorasaninejad, et al., Polarization-insensitive metalenses at visible wavelengths, Nano Lett. 16 (2016) 7229–7234, https://doi.org/10.1021/acs.nanolett.6b03626. PMID: 27791380.
[31] M. Khorasaninejad, et al., Metalenses at visible wavelengths: diffraction-limited focusing and subwavelength resolution imaging, Science 352 (2016) 1190–1194. https://www.science.org/doi/abs/10.1126/science.aaf6644.
[32] N. Yu, et al., Light propagation with phase discontinuities: generalized laws of reflection and refraction, Science 334 (2011) 333–337. https://www.science.org/doi/abs/10.1126/science.1210713.
[33] A. Arbabi, R.M. Briggs, Y. Horie, M. Bagheri, A. Faraon, Efficient dielectric metasurface collimating lenses for mid-infrared quantum cascade lasers, Opt Express 23 (2015) 33310–33317. https://opg.optica.org/oe/abstract.cfm?URI=oe-23-26-33310.
[34] M. Decker, et al., High-efficiency dielectric huygens' surfaces, Adv. Opt. Mater. 3 (2015) 813–820. https://onlinelibrary.wiley.com/doi/abs/10.1002/adom.201400584.
[35] Z. Liang, J. Li, Extreme acoustic metamaterial by coiling up space, Phys. Rev. Lett. 108 (2012): 114301. https://link.aps.org/doi/10.1103/PhysRevLett.108.114301.
[36] Y. Li, et al., Acoustic focusing by coiling up space, Appl. Phys. Lett. 101 (2012): 233508, https://doi.org/10.1063/1.4769984.
[37] Y. Xie, B.-I. Popa, L. Zigoneanu, S.A. Cummer, Measurement of a broadband negative index with space-coiling acoustic metamaterials, Phys. Rev. Lett. 110 (2013): 175501. https://link.aps.org/doi/10.1103/PhysRevLett.110.175501.
[38] Y. Xie, et al., Wavefront modulation and subwavelength diffractive acoustics with an acoustic metasurface, Nat. Commun. 5 (2014) 5553.
[39] J. Zhao, B. Li, Z. Chen, C.-W. Qiu, Manipulating acoustic wavefront by inhomogeneous impedance and steerable extraordinary reflection, Sci. Rep. 3 (2013) 2537.
[40] Y. Li, B. Liang, Z.-M. Gu, X.-Y. Zou, J.-C. Cheng, Reflected wavefront manipulation based on ultrathin planar acoustic metasurfaces, Sci. Rep. 3 (2013) 2546.
[41] S.-W. Fan, et al., Tunable broadband reflective acoustic metasurface, Phys. Rev. Appl. 11 (2019): 044038. https://link.aps.org/doi/10.1103/PhysRevApplied.11.044038.
[42] N. Fang, et al., Ultrasonic metamaterials with negative modulus, Nat. Mater. 5 (2006) 452–456.
[43] Y. Li, X. Jiang, B. Liang, J.-C. Cheng, L. Zhang, Metascreen-based acoustic passive phased array, Phys. Rev. Appl. 4 (2015): 024003. https://link.aps.org/doi/10.1103/PhysRevApplied.4.024003.
[44] S. Tang, B. Ren, Y. Feng, J. Song, Y. Jiang, Broadband acoustic focusing via binary rectangular cavity/Helmholtz resonator metasurface, J. Appl. Phys. 129 (2021): 155307, https://doi.org/10.1063/5.0049407.
[45] R. Martínez-Sala, et al., Sound attenuation by sculpture, Nature 378 (1995) 241, 241.
[46] D. Lee, D.M. Nguyen, J. Rho, Acoustic wave science realized by metamaterials, Nano convergence 4 (2017) 1–15.
[47] D. Lee, C. Cho, J. Mun, N. Park, J. Rho, Demonstration of steering acoustic waves by generalized Eaton lens, Appl. Phys. Lett. 113 (2018): 161904, https://doi.org/10.1063/1.5051439.
[48] S. Yang, et al., Focusing of sound in a 3d phononic crystal, Phys. Rev. Lett. 93 (2004): 024301. https://link.aps.org/doi/10.1103/PhysRevLett.93.024301.
[49] G. Lee, et al., Multiband elastic wave energy localization for highly amplified piezoelectric energy harvesting using trampoline metamaterials, Mech. Syst. Signal Process. 200 (2023): 110593. https://www.sciencedirect.com/science/article/pii/S0888327023005010.
[50] A. Allam, K. Sabra, A. Erturk, 3d-printed gradient-index phononic crystal lens for underwater acoustic wave focusing, Phys. Rev. Appl. 13 (2020): 064064. https://link.aps.org/doi/10.1103/PhysRevApplied.13.064064.
[51] G. Lee, et al., Piezoelectric energy harvesting using mechanical metamaterials and phononic crystals, Commun. Phys. 5 (2022) 94.
[52] D. Lee, M. Kim, J. Rho, A finite element method towards acoustic phononic crystals by weak formulation, J. Phys. Condens. Matter 31 (2019): 375901, https://doi.org/10.1088/1361-648X/ab2700.
[53] M. Lawrence, et al., High quality factor phase gradient metasurfaces, Nat. Nanotechnol. 15 (2020) 956–961.
[54] A.C. Overvig, S.C. Malek, N. Yu, Multifunctional nonlocal metasurfaces, Phys. Rev. Lett. 125 (2020): 017402. https://link.aps.org/doi/10.1103/PhysRevLett.125.017402.
[55] L. Quan, A. Alù, Passive acoustic metasurface with unitary reflection based on nonlocality, Phys. Rev. Appl. 11 (2019): 054077. https://link.aps.org/doi/10.1103/PhysRevApplied.11.054077.
[56] X. Fang, et al., Observation of higher-order exceptional points in a non-local acoustic metagrating, Commun. Phys. 4 (2021) 271.
[57] K. Shastri, F. Monticone, Nonlocal flat optics, Nat. Photonics 17 (2023) 36–47.
[58] Z. Li, et al., Flexible confinement and manipulation of mie resonances via nano rectangular hollow metasurfaces, Adv. Opt. Mater. 10 (2022): 2200185. https://onlinelibrary.wiley.com/doi/abs/10.1002/adom.202200185.
[59] Z. Wang, et al., On-chip wavefront shaping with dielectric metasurface, Nat. Commun. 10 (2019) 3547.
[60] H. Kwon, D. Sounas, A. Cordaro, A. Polman, A. Alù, Nonlocal metasurfaces for optical signal processing, Phys. Rev. Lett. 121 (2018): 173004. https://link.aps.org/doi/10.1103/PhysRevLett.121.173004.
[61] R. Chai, et al., Emerging planar nanostructures involving both local and nonlocal modes, ACS Photonics 10 (2023) 2031–2044, https://doi.org/10.1021/acsphotonics.2c01534.
[62] A.C. Overvig, S.C. Malek, M.J. Carter, S. Shrestha, N. Yu, Selection rules for quasibound states in the continuum, Phys. Rev. B 102 (2020): 035434. https://link.aps.org/doi/10.1103/PhysRevB.102.035434.
[63] S.C. Malek, A.C. Overvig, A. Alù, N. Yu, Multifunctional resonant wavefront-shaping meta-optics based on multilayer and multi-perturbation nonlocal metasurfaces, Light Sci. Appl. 11 (2022) 246.
[64] J.-H. Song, J. van de Groep, S.J. Kim, M.L. Brongersma, Non-local metasurfaces for spectrally decoupled wavefront manipulation and eye tracking, Nat. Nanotechnol. 16 (2021) 1224–1230.
[65] E. Klopfer, M. Lawrence, D.R.I. Barton, J. Dixon, J.A. Dionne, Dynamic focusing with high-quality-factor metalenses, Nano Lett. 20 (2020) 5127–5132, https://doi.org/10.1021/acs.nanolett.0c01359. PMID: 32497434.
[66] L. Quan, A. Alù, Hyperbolic sound propagation over nonlocal acoustic metasurfaces, Phys. Rev. Lett. 123 (2019): 244303. https://link.aps.org/doi/10.1103/PhysRevLett.123.244303.
[67] A. Díaz-Rubio, S.A. Tretyakov, Acoustic metasurfaces for scattering-free anomalous reflection and refraction, Phys. Rev. B 96 (2017): 125409. https://link.aps.org/doi/10.1103/PhysRevB.96.125409.
[68] X. Wang, R. Dong, Y. Li, Y. Jing, Non-local and non-hermitian acoustic metasurfaces, Rep. Prog. Phys. 86 (2023): 116501, https://doi.org/10.1088/1361-6633/acfbeb.
[69] A. Overvig, A. Alù, Diffractive nonlocal metasurfaces, Laser Photon. Rev. 16 (2022): 2100633. https://onlinelibrary.wiley.com/doi/abs/10.1002/lpor.202100633.
[70] E. Bayati, A. Zhan, S. Colburn, M.V. Zhelyeznyakov, A. Majumdar, Role of refractive index in metalens performance, Appl. Opt. 58 (2019) 1460–1466. https://opg.optica.org/ao/abstract.cfm?URI=ao-58-6-1460.
[71] M.-H. Chen, et al., Polarization-insensitive gan metalenses at visible wavelengths, Sci. Rep. 11 (2021): 14541.
[72] S. Shrestha, A.C. Overvig, M. Lu, A. Stein, N. Yu, Broadband achromatic dielectric metalenses, Light Sci. Appl. 7 (2018) 85.
[73] H. Liang, et al., Ultrahigh numerical aperture metalens at visible wavelengths, Nano Lett. 18 (2018) 4460–4466, https://doi.org/10.1021/acs.nanolett.8b01570. PMID: 29940122.
[74] Y. Yang, et al., Revealing structural disorder in hydrogenated amorphous silicon for a low-loss photonic platform at visible frequencies, Adv. Mater. 33 (2021): 2005893. https://onlinelibrary.wiley.com/doi/abs/10.1002/adma.202005893.
[75] D. Zhao, et al., Recent advances in ultraviolet nanophotonics: from plasmonics and metamaterials to metasurfaces, Nanophotonics 10 (2021) 2283–2308, https://doi.org/10.1515/nanoph-2021-0083.
[76] J. Kim, et al., Photonic encryption platform via dual-band vectorial metaholograms in the ultraviolet and visible, ACS Nano 16 (2022) 3546–3553, https://doi.org/10.1021/acsnano.1c10100. PMID: 35184548.
[77] K. Huang, et al., Ultraviolet metasurfaces of ≈ 80% efficiency with antiferromagnetic resonances for optical vectorial anti-counterfeiting, Laser Photon. Rev. 13 (2019): 1800289. https://onlinelibrary.wiley.com/doi/abs/10.1002/lpor.201800289.

[78] L. Guo, et al., Design of aluminum nitride metalens for broadband ultraviolet incidence routing, Nanophotonics 8 (2019) 171–180, https://doi.org/10.1515/nanoph-2018-0151.
[79] C. Zhang, et al., Low-loss metasurface optics down to the deep ultraviolet region, Light Sci. Appl. 9 (2020) 55.
[80] J. Kim, et al., One-step printable platform for high-efficiency metasurfaces down to the deep-ultraviolet region, Light Sci. Appl. 12 (2023) 68.
[81] A.H. Dorrah, F. Capasso, Tunable structured light with flat optics, Science 376 (2022) eabi6860. https://www.science.org/doi/abs/10.1126/science.abi6860.
[82] A. Arbabi, A. Faraon, Advances in optical metalenses, Nat. Photonics 17 (2023) 16–25.
[83] D. Jeon, K. Shin, S.-W. Moon, J. Rho, Recent advancements of metalenses for functional imaging, Nano Convergence 10 (2023) 1–26.
[84] S.-W. Moon, et al., Tutorial on metalenses for advanced flat optics: design, fabrication, and critical considerations, J. Appl. Phys. 131 (2022): 091101, https://doi.org/10.1063/5.0078804.
[85] W.T. Chen, et al., Immersion meta-lenses at visible wavelengths for nanoscale imaging, Nano Lett. 17 (2017) 3188–3194, https://doi.org/10.1021/acs.nanolett.7b00717. PMID: 28388086.
[86] P. Lalanne, P. Chavel, Metalenses at visible wavelengths: past, present, perspectives, Laser Photon. Rev. 11 (2017): 1600295. https://onlinelibrary.wiley.com/doi/abs/10.1002/lpor.201600295.
[87] Z. Li, R. Pestourie, Z. Lin, S.G. Johnson, F. Capasso, Empowering metasurfaces with inverse design: principles and applications, ACS Photonics 9 (2022) 2178–2192, https://doi.org/10.1021/acsphotonics.1c01850.
[88] J. Park, et al., Free-form optimization of nanophotonic devices: from classical methods to deep learning, Nanophotonics 11 (2022) 1809–1845, https://doi.org/10.1515/nanoph-2021-0713.
[89] M. Mansouree, A. McClung, S. Samudrala, A. Arbabi, Large-scale parametrized metasurface design using adjoint optimization, ACS Photonics 8 (2021) 455–463, https://doi.org/10.1021/acsphotonics.0c01058.
[90] D. Sang, et al., Toward high-efficiency ultrahigh numerical aperture freeform metalens: from vector diffraction theory to topology optimization, Laser Photon. Rev. 16 (2022): 2200265. https://onlinelibrary.wiley.com/doi/abs/10.1002/lpor.202200265.
[91] Y. Ra'di, D.L. Sounas, A. Metagratings Alù, Beyond the limits of graded metasurfaces for wave front control, Phys. Rev. Lett. 119 (2017): 067404. https://link.aps.org/doi/10.1103/PhysRevLett.119.067404.
[92] Y. Ra'di, A. Alù, Metagratings for efficient wavefront manipulation, IEEE Photon. J. 14 (2022) 1–13.
[93] R. Paniagua-Domínguez, et al., A metalens with a near-unity numerical aperture, Nano Lett. 18 (2018) 2124–2132, https://doi.org/10.1021/acs.nanolett.8b00368. PMID: 29485885.
[94] J. Zhang, et al., Metalenses with polarization-insensitive adaptive nano-antennas, Laser Photon. Rev. 16 (2022): 2200268. https://onlinelibrary.wiley.com/doi/abs/10.1002/lpor.202200268.
[95] D. Sell, J. Yang, S. Doshay, R. Yang, J.A. Fan, Large-angle, multifunctional metagratings based on freeform multimode geometries, Nano Lett. 17 (2017) 3752–3757, https://doi.org/10.1021/acs.nanolett.7b01082. PMID: 28459583.
[96] J. Jiang, et al., Free-form diffractive metagrating design based on generative adversarial networks, ACS Nano 13 (2019) 8872–8878, https://doi.org/10.1021/acsnano.9b02371. PMID: 31314492.
[97] M. Plidschun, et al., Ultrahigh numerical aperture meta-fibre for flexible optical trapping, Light Sci. Appl. 10 (2021) 57.
[98] W. Hadibrata, H. Wei, S. Krishnaswamy, K. Aydin, Inverse design and 3d printing of a metalens on an optical fiber tip for direct laser lithography, Nano Lett. 21 (2021) 2422–2428, https://doi.org/10.1021/acs.nanolett.0c04463. PMID: 33720738.
[99] J. Xiao, T. Plaskocinski, M. Biabanifard, S. Persheyev, A. Di Falco, On-chip optical trapping with high na metasurfaces, ACS Photonics 10 (2023) 1341–1348, https://doi.org/10.1021/acsphotonics.2c01986.
[100] F. Yang, et al., Wide field-of-view metalens: a tutorial, Advanced Photonics 5 (2023): 033001, https://doi.org/10.1117/1.AP.5.3.033001.
[101] X. Luo, et al., Recent advances of wide-angle metalenses: principle, design, and applications, Nanophotonics 11 (2022) 1–20, https://doi.org/10.1515/nanoph-2021-0583.
[102] F. Aieta, P. Genevet, M. Kats, F. Capasso, Aberrations of flat lenses and aplanatic metasurfaces, Opt Express 21 (2013) 31530–31539. https://opg.optica.org/oe/abstract.cfm?URI=oe-21-25-31530.
[103] A. Kalvach, Z. Szabó, Aberration-free flat lens design for a wide range of incident angles, J. Opt. Soc. Am. B 33 (2016) A66–A71. https://opg.optica.org/josab/abstract.cfm?URI=josab-33-2-A66.
[104] H. Liang, et al., High performance metalenses: numerical aperture, aberrations, chromaticity, and trade-offs, Optica 6 (2019) 1461–1470. https://opg.optica.org/optica/abstract.cfm?URI=optica-6-12-1461.
[105] M. Pan, et al., Dielectric metalens for miniaturized imaging systems: progress and challenges, Light Sci. Appl. 11 (2022) 195.
[106] J. Engelberg, et al., Near-ir wide-field-of-view huygens metalens for outdoor imaging applications, Nanophotonics 9 (2020) 361–370, https://doi.org/10.1515/nanoph-2019-0177.
[107] M.Y. Shalaginov, et al., Single-element diffraction-limited fisheye metalens, Nano Lett. 20 (2020) 7429–7437, https://doi.org/10.1021/acs.nanolett.0c02783. PMID: 32942862.
[108] F. Zhang, et al., Extreme-angle silicon infrared optics enabled by streamlined surfaces, Adv. Mater. 33 (2021): 2008157. https://onlinelibrary.wiley.com/doi/abs/10.1002/adma.202008157.
[109] A. Martins, et al., On metalenses with arbitrarily wide field of view, ACS Photonics 7 (2020) 2073–2079, https://doi.org/10.1021/acsphotonics.0c00479.
[110] C. Hao, et al., Single-layer aberration-compensated flat lens for robust wide-angle imaging, Laser Photon. Rev. 14 (2020): 2000017. https://onlinelibrary.wiley.com/doi/abs/10.1002/lpor.202000017.
[111] A. Arbabi, et al., Miniature optical planar camera based on a wide-angle metasurface doublet corrected for monochromatic aberrations, Nat. Commun. 7 (2016): 13682.
[112] M. Pu, X. Li, Y. Guo, X. Ma, X. Luo, Nanoapertures with ordered rotations: symmetry transformation and wide-angle flat lensing, Opt Express 25 (2017) 31471–31477. https://opg.optica.org/oe/abstract.cfm?URI=oe-25-25-31471.
[113] E. Lassalle, et al., Imaging properties of large field-of-view quadratic metalenses and their applications to fingerprint detection, ACS Photonics 8 (2021) 1457–1468, https://doi.org/10.1021/acsphotonics.1c00237.
[114] H. Suo, et al., Wide-angle and high-efficiency flat retroreflector, Opt Express 30 (2022) 27249–27258. https://opg.optica.org/oe/abstract.cfm?URI=oe-30-15-27249.
[115] A. Martins, et al., Correction of aberrations via polarization in single layer metalenses, Adv. Opt. Mater. 10 (2022): 2102555. https://onlinelibrary.wiley.com/doi/abs/10.1002/adom.202102555.
[116] Y. Guo, et al., Spin-decoupled metasurface for simultaneous detection of spin and orbital angular momenta via momentum transformation, Light Sci. Appl. 10 (2021) 63.
[117] B. Groever, W.T. Chen, F. Capasso, Meta-lens doublet in the visible region, Nano Lett. 17 (2017) 4902–4907, https://doi.org/10.1021/acs.nanolett.7b01888. PMID: 28661676.
[118] Z. Lin, B. Groever, F. Capasso, A.W. Rodriguez, M. Lončar, Topology-optimized multilayered metaoptics, Phys. Rev. Appl. 9 (2018): 044030. https://link.aps.org/doi/10.1103/PhysRevApplied.9.044030.
[119] A. Martins, J. Li, B.-H.V. Borges, T.F. Krauss, E.R. Martins, Fundamental limits and design principles of doublet metalenses, Nanophotonics 11 (2022) 1187–1194, https://doi.org/10.1515/nanoph-2021-0770.
[120] Z. Huang, M. Qin, X. Guo, C. Yang, S. Li, Achromatic and wide-field metalens in the visible region, Opt Express 29 (2021) 13542–13551. https://opg.optica.org/oe/abstract.cfm?URI=oe-29-9-13542.
[121] D. Tang, L. Chen, J. Liu, X. Zhang, Achromatic metasurface doublet with a wide incident angle for light focusing, Opt Express 28 (2020) 12209–12218. https://opg.optica.org/oe/abstract.cfm?URI=oe-28-8-12209.
[122] C. Kim, S.-J. Kim, B. Lee, Doublet metalens design for high numerical aperture and simultaneous correction of chromatic and monochromatic aberrations, Opt Express 28 (2020) 18059–18076. https://opg.optica.org/oe/abstract.cfm?URI=oe-28-12-18059.
[123] Z. Li, et al., Super-oscillatory metasurface doublet for sub-diffraction focusing with a large incident angle, Opt Express 29 (2021) 9991–9999. https://opg.optica.org/oe/abstract.cfm?URI=oe-29-7-9991.
[124] Y. Wei, et al., Compact optical polarization-insensitive zoom metalens doublet, Adv. Opt. Mater. 8 (2020): 2000142. https://onlinelibrary.wiley.com/doi/abs/10.1002/adom.202000142.
[125] Y. Liu, et al., Meta-objective with sub-micrometer resolution for microendoscopes, Photon. Res. 9 (2021) 106–115. https://opg.optica.org/prj/abstract.cfm?URI=prj-9-2-106.
[126] F. Aieta, M.A. Kats, P. Genevet, F. Capasso, Multiwavelength achromatic metasurfaces by dispersive phase compensation, Science 347 (2015) 1342–1345. https://www.science.org/doi/abs/10.1126/science.aaa2494.
[127] S. Wang, et al., Broadband achromatic optical metasurface devices, Nat. Commun. 8 (2017) 187.
[128] S. Wang, et al., A broadband achromatic metalens in the visible, Nat. Nanotechnol. 13 (2018) 227–232.
[129] W.T. Chen, et al., A broadband achromatic metalens for focusing and imaging in the visible, Nat. Nanotechnol. 13 (2018) 220–226.
[130] S. Baek, et al., High numerical aperture rgb achromatic metalens in the visible, Photon. Res. 10 (2022) B30–B39. https://opg.optica.org/prj/abstract.cfm?URI=prj-10-12-B30.
[131] W. Feng, et al., Rgb achromatic metalens doublet for digital imaging, Nano Lett. 22 (2022) 3969–3975, https://doi.org/10.1021/acs.nanolett.2c00486. PMID: 35506587.
[132] F. Balli, M. Sultan, S.K. Lami, J.T. Hastings, A hybrid achromatic metalens, Nat. Commun. 11 (2020) 3892.
[133] Z. Li, et al., Inverse design enables large-scale high-performance meta-optics reshaping virtual reality, Nat. Commun. 13 (2022) 2409.
[134] H. Ren, et al., An achromatic metafiber for focusing and imaging across the entire telecommunication range, Nat. Commun. 13 (2022) 4183.
[135] E. Arbabi, A. Arbabi, S.M. Kamali, Y. Horie, A. Faraon, Multiwavelength metasurfaces through spatial multiplexing, Sci. Rep. 6 (2016): 32803.
[136] O. Avayu, E. Almeida, Y. Prior, T. Ellenbogen, Composite functional metasurfaces for multispectral achromatic optics, Nat. Commun. 8 (2017): 14992.
[137] Y. Zhou, et al., Multilayer noninteracting dielectric metasurfaces for multiwavelength metaoptics, Nano Lett. 18 (2018) 7529–7537, https://doi.org/10.1021/acs.nanolett.8b03017. PMID: 30394751.
[138] H. Chung, O.D. Miller, High-na achromatic metalenses by inverse design, Opt Express 28 (2020) 6945–6965. https://opg.optica.org/oe/abstract.cfm?URI=oe-28-5-6945.
[139] Y. Luo, et al., Meta-lens light-sheet fluorescence microscopy for in vivo imaging, Nanophotonics 11 (2022) 1949–1959, https://doi.org/10.1515/nanoph-2021-0748.

[140] Y. Wang, et al., High-efficiency broadband achromatic metalens for near-ir biological imaging window, Nat. Commun. 12 (2021) 5560.
[141] P. Lin, et al., Coherent Raman scattering imaging with a near-infrared achromatic metalens, APL Photonics 6 (2021): 096107, https://doi.org/10.1063/5.0059874.
[142] X. Feng, et al., Optical multiparameter detection system based on a broadband achromatic metalens array, Adv. Opt. Mater. 9 (2021): 2100772. https://onlinelibrary.wiley.com/doi/abs/10.1002/adom.202100772.
[143] R.J. Lin, et al., Achromatic metalens array for full-colour light-field imaging, Nat. Nanotechnol. 14 (2019) 227–231.
[144] Z.-B. Fan, et al., A broadband achromatic metalens array for integral imaging in the visible, Light Sci. Appl. 8 (2019) 67.
[145] J. Xiong, E.-L. Hsiang, Z. He, T. Zhan, S.-T. Wu, Augmented reality and virtual reality displays: emerging technologies and future perspectives, Light Sci. Appl. 10 (2021) 216.
[146] Z. Li, et al., Meta-optics achieves rgb-achromatic focusing for virtual reality, Sci. Adv. 7 (2021): eabe4458. https://www.science.org/doi/abs/10.1126/sciadv.abe4458.
[147] G.T. Haar, C. Coussios, High intensity focused ultrasound: physical principles and devices, Int. J. Hyperther. 23 (2007) 89–104, https://doi.org/10.1080/02656730601186138. PMID: 17578335.
[148] J. Li, C. Shen, A. Díaz-Rubio, S.A. Tretyakov, S.A. Cummer, Systematic design and experimental demonstration of bianisotropic metasurfaces for scattering-free manipulation of acoustic wavefronts, Nat. Commun. 9 (2018) 1342.
[149] Y.K. Chiang, et al., Scalable metagrating for efficient ultrasonic focusing, Phys. Rev. Appl. 16 (2021): 064014. https://link.aps.org/doi/10.1103/PhysRevApplied.16.064014.
[150] L. Fan, J. Mei, Flow-permeable and tunable metalens for subdiffraction waterborne-sound focusing, Phys. Rev. Appl. 19 (2023): 024026. https://link.aps.org/doi/10.1103/PhysRevApplied.19.024026.
[151] H. Xie, Z. Hou, Nonlocal metasurface for acoustic focusing, Phys. Rev. Appl. 15 (2021): 034054. https://link.aps.org/doi/10.1103/PhysRevApplied.15.034054.
[152] H.-W. Dong, et al., Achromatic metasurfaces by dispersion customization for ultra-broadband acoustic beam engineering, Natl. Sci. Rev. 9 (2022) nwac030, https://doi.org/10.1093/nsr/nwac030.
[153] X. Fan, et al., Ultrabroadband and reconfigurable transmissive acoustic metascreen, Adv. Funct. Mater. 33 (2023): 2300752. https://onlinelibrary.wiley.com/doi/abs/10.1002/adfm.202300752.
[154] C. Kim, J. Kim, W. Jeon, Realization of an acoustic metalens exhibiting broadband high transmission, J. Sound Vib. 529 (2022): 116910. https://www.sciencedirect.com/science/article/pii/S0022460X22001481.
[155] Z. Jia, J. Li, C. Shen, Y. Xie, S.A. Cummer, Systematic design of broadband path-coiling acoustic metamaterials, J. Appl. Phys. 123 (2018): 025101, https://doi.org/10.1063/1.5009488.
[156] Y. Zhu, B. Assouar, Multifunctional acoustic metasurface based on an array of helmholtz resonators, Phys. Rev. B 99 (2019): 174109. https://link.aps.org/doi/10.1103/PhysRevB.99.174109.
[157] J. Qian, et al., Broadband acoustic focusing by cavity structures with phase manipulations, J. Appl. Phys. 122 (2017): 244501, https://doi.org/10.1063/1.4998223.
[158] R. Al Jahdali, Y. Wu, High transmission acoustic focusing by impedance-matched acoustic meta-surfaces, Appl. Phys. Lett. 108 (2016): 031902, https://doi.org/10.1063/1.4939932.
[159] J. Chen, J. Rao, D. Lisevych, Z. Fan, Broadband ultrasonic focusing in water with an ultra-compact metasurface lens, Appl. Phys. Lett. 114 (2019): 104101, https://doi.org/10.1063/1.5090956.
[160] N.-L. Zhang, S.-D. Zhao, H.-W. Dong, Y.-S. Wang, C. Zhang, Reflection-type broadband coding metasurfaces for acoustic focusing and splitting, Appl. Phys. Lett. 120 (2022): 142201, https://doi.org/10.1063/5.0087339.
[161] T. Liu, F. Chen, S. Liang, H. Gao, J. Zhu, Subwavelength sound focusing and imaging via gradient metasurface-enabled spoof surface acoustic wave modulation, Phys. Rev. Appl. 11 (2019): 034061. https://link.aps.org/doi/10.1103/PhysRevApplied.11.034061.
[162] J.-P. Xia, et al., Broadband tunable acoustic asymmetric focusing lens from dual-layer metasurfaces, Phys. Rev. Appl. 10 (2018): 014016. https://link.aps.org/doi/10.1103/PhysRevApplied.10.014016.
[163] R. Ghaffarivardavagh, J. Nikolajczyk, R. Glynn Holt, S. Anderson, X. Zhang, Horn-like space-coiling metamaterials toward simultaneous phase and amplitude modulation, Nat. Commun. 9 (2018) 1349.
[164] S. Qi, B. Assouar, Ultrathin acoustic metasurfaces for reflective wave focusing, J. Appl. Phys. 123 (2018): 234501, https://doi.org/10.1063/1.5031482.
[165] J. Chen, J. Xiao, D. Lisevych, A. Shakouri, Z. Fan, Deep-subwavelength control of acoustic waves in an ultra-compact metasurface lens, Nat. Commun. 9 (2018) 4920.
[166] C. Jung, et al., Metasurface-driven optically variable devices, Chem. Rev. 121 (2021) 13013–13050, https://doi.org/10.1021/acs.chemrev.1c00294. PMID: 34491723.
[167] T. Badloe, J. Lee, J. Seong, J. Rho, Tunable metasurfaces: the path to fully active nanophotonics, Advanced Photonics Research 2 (2021): 2000205. https://onlinelibrary.wiley.com/doi/abs/10.1002/adpr.202000205.
[168] T. Cui, B. Bai, H.-B. Sun, Tunable metasurfaces based on active materials, Adv. Funct. Mater. 29 (2019): 1806692. https://onlinelibrary.wiley.com/doi/abs/10.1002/adfm.201806692.
[169] J. Kim, et al., Tunable metasurfaces towards versatile metalenses and metaholograms: a review, Advanced Photonics 4 (2022): 024001, https://doi.org/10.1117/1.AP.4.2.024001.
[170] I. Kim, et al., Stimuli-responsive dynamic metaholographic displays with designer liquid crystal modulators, Adv. Mater. 32 (2020): 2004664. https://onlinelibrary.wiley.com/doi/abs/10.1002/adma.202004664.
[171] C. Jung, et al., Disordered-nanoparticle–based etalon for ultrafast humidity-responsive colorimetric sensors and anti-counterfeiting displays, Sci. Adv. 8 (2022): eabm8598. https://www.science.org/doi/abs/10.1126/sciadv.abm8598.
[172] B. Ko, et al., Humidity-responsive rgb-pixels via swelling of 3d nanoimprinted polyvinyl alcohol, Adv. Sci. 10 (2023): 2204469. https://onlinelibrary.wiley.com/doi/abs/10.1002/advs.202204469.
[173] T. Badloe, et al., Liquid crystal-powered mie resonators for electrically tunable photorealistic color gradients and dark blacks, Light Sci. Appl. 11 (2022) 118.
[174] A. Zabihi, C. Ellouzi, C. Shen, Tunable, reconfigurable, and programmable acoustic metasurfaces: a review, Frontiers in Materials 10 (2023). https://www.frontiersin.org/articles/10.3389/fmats.2023.1132585.
[175] Q. Guo, et al., Compact single-shot metalens depth sensors inspired by eyes of jumping spiders, Proc. Natl. Acad. Sci. USA 116 (2019) 22959–22965. https://www.pnas.org/doi/abs/10.1073/pnas.1912154116.
[176] T. Badloe, I. Kim, Y. Kim, J. Kim, J. Rho, Electrically tunable bifocal metalens with diffraction-limited focusing and imaging at visible wavelengths, Adv. Sci. 8 (2021): 2102646. https://onlinelibrary.wiley.com/doi/abs/10.1002/advs.202102646.
[177] C. Chen, et al., Parallel polarization illumination with a multifocal axicon metalens for improved polarization imaging, Nano Lett. 20 (2020) 5428–5434, https://doi.org/10.1021/acs.nanolett.0c01877. PMID: 32584049.
[178] M. Khorasaninejad, et al., Multispectral chiral imaging with a metalens, Nano Lett. 16 (2016) 4595–4600, https://doi.org/10.1021/acs.nanolett.6b01897. PMID: 27267137.
[179] T. Badloe, J. Seong, J. Rho, Trichannel spin-selective metalenses, Nano Lett. 23 (2023) 6958–6965, https://doi.org/10.1021/acs.nanolett.3c01588. PMID: 37478358.
[180] A.Y. Zhu, et al., Ultra-compact visible chiral spectrometer with meta-lenses, APL Photonics 2 (2017): 036103, https://doi.org/10.1063/1.4974259.
[181] R. Wang, et al., Compact multi-foci metalens spectrometer, Light Sci. Appl. 12 (2023) 103.
[182] E. Arbabi, S.M. Kamali, A. Arbabi, A. Faraon, Full-Stokes imaging polarimetry using dielectric metasurfaces, ACS Photonics 5 (2018) 3132–3140, https://doi.org/10.1021/acsphotonics.8b00362.
[183] T. Badloe, et al., Bright-field and edge-enhanced imaging using an electrically tunable dual-mode metalens, ACS Nano 17 (2023) 14678–14685, https://doi.org/10.1021/acsnano.3c02471. PMID: 37490514.
[184] So, S., Mun, J., Park, J. & Rho, J. Revisiting the design strategies for metasurfaces: Fundamental physics, optimization, and beyond. Advanced Materials n/a, 2206399. URL https://onlinelibrary.wiley.com/doi/abs/10.1002/adma.202206399.
[185] E. Arbabi, et al., Mems-tunable dielectric metasurface lens, Nat. Commun. 9 (2018) 812.
[186] S. Wei, et al., A varifocal graphene metalens for broadband zoom imaging covering the entire visible region, ACS Nano 15 (2021) 4769–4776, https://doi.org/10.1021/acsnano.0c09395. PMID: 33593050.
[187] Y. Luo, et al., Varifocal metalens for optical sectioning fluorescence microscopy, Nano Lett. 21 (2021) 5133–5142, https://doi.org/10.1021/acs.nanolett.1c01114. PMID: 34097419.
[188] M. Wang, et al., Varifocal metalens using tunable and ultralow-loss dielectrics, Adv. Sci. 10 (2023): 2204899. https://onlinelibrary.wiley.com/doi/abs/10.1002/advs.202204899.
[189] Z. Shen, et al., Liquid crystal integrated metalens with tunable chromatic aberration, Advanced Photonics 2 (2020): 036002, https://doi.org/10.1117/1.AP.2.3.036002.
[190] Z. Zhang, X. Qi, J. Zhang, C. Guo, Z. Zhu, Graphene-enabled electrically tunability of metalens in the terahertz range, Opt Express 28 (2020) 28101–28112. https://opg.optica.org/oe/abstract.cfm?URI=oe-28-19-28101.
[191] H.-S. Ee, R. Agarwal, Tunable metasurface and flat optical zoom lens on a stretchable substrate, Nano Lett. 16 (2016) 2818–2823, https://doi.org/10.1021/acs.nanolett.6b00618. PMID: 26986191.
[192] K.-K. Du, et al., Control over emissivity of zero-static-power thermal emitters based on phase-changing material gst, Light Sci. Appl. 6 (2017): e16194–e16194.
[193] M.Y. Shalaginov, et al., Reconfigurable all-dielectric metalens with diffraction-limited performance, Nat. Commun. 12 (2021) 1225.
[194] S. Park, et al., Electrically focus-tuneable ultrathin lens for high-resolution square subpixels, Light Sci. Appl. 9 (2020) 98.
[195] A. Forouzmand, H. Mosallaei, A tunable semiconductor-based transmissive metasurface: dynamic phase control with high transmission level, Laser Photon. Rev. 14 (2020): 1900353. https://onlinelibrary.wiley.com/doi/abs/10.1002/lpor.201900353.
[196] A. Olivieri, et al., Plasmonic nanostructured metal–oxide–semiconductor reflection modulators, Nano Lett. 15 (2015) 2304–2311, https://doi.org/10.1021/nl504389f. PMID: 25730698.
[197] Y.-W. Huang, et al., Gate-tunable conducting oxide metasurfaces, Nano Lett. 16 (2016) 5319–5325, https://doi.org/10.1021/acs.nanolett.6b00555. PMID: 27564012.
[198] J. Park, et al., All-solid-state spatial light modulator with independent phase and amplitude control for three-dimensional lidar applications, Nat. Nanotechnol. 16 (2021) 69–76.
[199] M. Klein, et al., Polarization-tunable perovskite light-emitting metatransistor, Adv. Mater. 35 (2023): 2207317. https://onlinelibrary.wiley.com/doi/abs/10.1002/adma.202207317.

[200] C. Zhang, et al., A reconfigurable active acoustic metalens, Appl. Phys. Lett. 118 (2021): 133502, https://doi.org/10.1063/5.0045024.
[201] K. Gong, X. Wang, H. Ouyang, J. Mo, Tuneable gradient helmholtz-resonator-based acoustic metasurface for acoustic focusing, J. Phys. Appl. Phys. 52 (2019): 385303, https://doi.org/10.1088/1361-6463/ab2b85.
[202] Z. Tian, et al., Programmable acoustic metasurfaces, Adv. Funct. Mater. 29 (2019): 1808489. https://onlinelibrary.wiley.com/doi/abs/10.1002/adfm.201808489.
[203] S.-D. Zhao, A.-L. Chen, Y.-S. Wang, C. Zhang, Continuously tunable acoustic metasurface for transmitted wavefront modulation, Phys. Rev. Appl. 10 (2018): 054066. https://link.aps.org/doi/10.1103/PhysRevApplied.10.054066.
[204] Z. Li, et al., Coding piezoelectric metasurfaces, Adv. Funct. Mater. 32 (2022): 2209173. https://onlinelibrary.wiley.com/doi/abs/10.1002/adfm.202209173.
[205] P.-Q. Li, et al., Generating multistructured ultrasound via bioinspired metaskin patterning for low-threshold and contactless control of living organisms, Adv. Funct. Mater. 32 (2022): 2203109. https://onlinelibrary.wiley.com/doi/abs/10.1002/adfm.202203109.
[206] Y. Zhu, et al., Janus acoustic metascreen with nonreciprocal and reconfigurable phase modulations, Nat. Commun. 12 (2021) 7089.
[207] Y. Tang, et al., Transmission-reflection-integrated multifunctional continuously tunable metasurfaces for decoupled modulation of acoustic waves, Phys. Rev. Appl. 17 (2022): 044027. https://link.aps.org/doi/10.1103/PhysRevApplied.17.044027.
[208] B. Liu, Q. Wei, Z. Su, Y. Wang, L. Huang, Multifunctional acoustic holography based on compact acoustic geometric-phase meta-array, J. Appl. Phys. 131 (2022): 185108, https://doi.org/10.1063/5.0085562.
[209] X. Jiang, Y. Li, B. Liang, J.-c. Cheng, L. Zhang, Convert acoustic resonances to orbital angular momentum, Phys. Rev. Lett. 117 (2016): 034301. https://link.aps.org/doi/10.1103/PhysRevLett.117.034301.
[210] B. Liu, et al., Experimental verification of the acoustic geometric phase, Appl. Phys. Lett. 120 (2022): 211702, https://doi.org/10.1063/5.0091474.
[211] J. Yang, et al., Photonic crystal fiber metalens, Nanophotonics 8 (2019) 443–449, https://doi.org/10.1515/nanoph-2018-0204.
[212] X. Guo, Y. Ding, X. Chen, Y. Duan, X. Ni, Molding free-space light with guided wave–driven metasurfaces, Sci. Adv. 6 (2020) eabb4142. https://www.science.org/doi/abs/10.1126/sciadv.abb4142.
[213] R. Sawant, et al., Aberration-corrected large-scale hybrid metalenses, Optica 8 (2021) 1405–1411. https://opg.optica.org/optica/abstract.cfm?URI=optica-8-11-1405.
[214] Y.-Y. Xie, et al., Metasurface-integrated vertical cavity surface-emitting lasers for programmable directional lasing emissions, Nat. Nanotechnol. 15 (2020) 125–130.
[215] E. Khaidarov, et al., Control of led emission with functional dielectric metasurfaces, Laser Photon. Rev. 14 (2020): 1900235. https://onlinelibrary.wiley.com/doi/abs/10.1002/lpor.201900235.
[216] X. Hua, et al., Ultra-compact snapshot spectral light-field imaging, Nat. Commun. 13 (2022) 2732.
[217] Q. Fan, et al., Trilobite-inspired neural nanophotonic light-field camera with extreme depth-of-field, Nat. Commun. 13 (2022) 2130.
[218] M.K. Chen, et al., A meta-device for intelligent depth perception, Adv. Mater. 35 (2023): 2107465. https://onlinelibrary.wiley.com/doi/abs/10.1002/adma.202107465.
[219] L. Zhang, et al., High-efficiency, 80 mm aperture metalens telescope, Nano Lett. 23 (2023) 51–57, https://doi.org/10.1021/acs.nanolett.2c03561. PMID: 36525639.
[220] J. Kim, et al., Scalable manufacturing of high-index atomic layer–polymer hybrid metasurfaces for metaphotonics in the visible, Nat. Mater. 22 (2023) 474–481.
[221] T. Zhan, K. Yin, J. Xiong, Z. He, S.-T. Wu, Augmented reality and virtual reality displays: perspectives and challenges, iScience 23 (2020): 101397. https://www.sciencedirect.com/science/article/pii/S258900422030585X.
[222] G.-Y. Lee, et al., Metasurface eyepiece for augmented reality, Nat. Commun. 9 (2018) 4562.
[223] A. Leitis, M.L. Tseng, A. John-Herpin, Y.S. Kivshar, H. Altug, Wafer-scale functional metasurfaces for mid-infrared photonics and biosensing, Adv. Mater. 33 (2021): 2102232. https://onlinelibrary.wiley.com/doi/abs/10.1002/adma.202102232.
[224] J. Tao, et al., Mass-manufactured beam-steering metasurfaces for high-speed full-duplex optical wireless-broadcasting communications, Adv. Mater. 34 (2022): 2106080. https://onlinelibrary.wiley.com/doi/abs/10.1002/adma.202106080.
[225] H. Choi, et al., Realization of high aspect ratio metalenses by facile nanoimprint lithography using water-soluble stamps, PhotoniX 4 (2023) 1–11.
[226] H. Jia, et al., Subwavelength imaging by a simple planar acoustic superlens, Appl. Phys. Lett. 97 (2010): 173507, https://doi.org/10.1063/1.3507893.
[227] J. Zhu, et al., A holey-structured metamaterial for acoustic deep-subwavelength imaging, Nat. Phys. 7 (2011) 52–55.
[228] Y.-X. Shen, et al., Ultrasonic super-oscillation wave-packets with an acoustic meta-lens, Nat. Commun. 10 (2019) 3411.
[229] E.L. Walker, Y. Jin, D. Reyes, A. Neogi, Sub-wavelength lateral detection of tissue-approximating masses using an ultrasonic metamaterial lens, Nat. Commun. 11 (2020) 5967.
[230] X. Zhou, M. Badreddine Assouar, M. Oudich, Subwavelength acoustic focusing by surface-wave-resonance enhanced transmission in doubly negative acoustic metamaterials, J. Appl. Phys. 116 (2014).
[231] N. Kaina, F. Lemoult, M. Fink, G. Lerosey, Negative refractive index and acoustic superlens from multiple scattering in single negative metamaterials, Nature 525 (2015) 77–81.
[232] H. Lee, J.H. Oh, H.M. Seung, S.H. Cho, Y.Y. Kim, Extreme stiffness hyperbolic elastic metamaterial for total transmission subwavelength imaging, Sci. Rep. 6 (2016): 24026.
[233] J. Chen, Z. Sun, J. Rao, D. Lisevych, Z. Fan, Escalated deep-subwavelength acoustic imaging with field enhancement inside a metalens, Phys. Rev. Appl. 16 (2021): 044021. https://link.aps.org/doi/10.1103/PhysRevApplied.16.044021.
[234] P. Huo, et al., Photonic spin-multiplexing metasurface for switchable spiral phase contrast imaging, Nano Lett. 20 (2020) 2791–2798, https://doi.org/10.1021/acs.nanolett.0c00471. PMID: 32155076.
[235] B. Wang, D.C. Liu, A Novel Edge Enhancement Method for Ultrasound Imaging, IEEE, 2008, pp. 2414–2417.
[236] M. Molerón, C. Daraio, Acoustic metamaterial for subwavelength edge detection, Nat. Commun. 6 (2015) 8037.
[237] C. Ma, S. Kim, N.X. Fang, Far-field acoustic subwavelength imaging and edge detection based on spatial filtering and wave vector conversion, Nat. Commun. 10 (2019) 204.
[238] L. Li, Y. Diao, H. Wu, W. Jiang, Complementary acoustic metamaterial for penetrating aberration layers, ACS Appl. Mater. Interfaces 14 (2022) 28604–28614, https://doi.org/10.1021/acsami.2c06227. PMID: 35726703.
[239] S. Jiménez-Gambín, N. Jiménez, J.M. Benlloch, F. Camarena, Holograms to focus arbitrary ultrasonic fields through the skull, Phys. Rev. Appl. 12 (2019): 014016. https://link.aps.org/doi/10.1103/PhysRevApplied.12.014016.
[240] Z. Hu, Y. Yang, L. Xu, Y. Hao, H. Chen, Binary acoustic metasurfaces for dynamic focusing of transcranial ultrasound, Front. Neurosci. 16 (2022). https://www.frontiersin.org/articles/10.3389/fnins.2022.984953.
[241] A.C. Singer, J.K. Nelson, S.S. Kozat, Signal processing for underwater acoustic communications, IEEE Commun. Mag. 47 (2009) 90–96.
[242] C. Shi, M. Dubois, Y. Wang, X. Zhang, High-speed acoustic communication by multiplexing orbital angular momentum, Proc. Natl. Acad. Sci. USA 114 (2017) 7250–7253. https://www.pnas.org/doi/abs/10.1073/pnas.1704450114.
[243] X. Jiang, B. Liang, J.-C. Cheng, C.-W. Qiu, Twisted acoustics: metasurface-enabled multiplexing and demultiplexing, Adv. Mater. 30 (2018): 1800257. https://onlinelibrary.wiley.com/doi/abs/10.1002/adma.201800257.
[244] K. Wu, et al., Metamaterial-based real-time communication with high information density by multipath twisting of acoustic wave, Nat. Commun. 13 (2022) 5171.
[245] E. Bok, et al., Metasurface for water-to-air sound transmission, Phys. Rev. Lett. 120 (2018): 044302. https://link.aps.org/doi/10.1103/PhysRevLett.120.044302.
[246] J. Liu, Z. Li, B. Liang, J.-C. Cheng, A. Alù, Remote water-to-air eavesdropping with a phase-engineered impedance matching metasurface, Adv. Mater. 35 (2023): 2301799. https://onlinelibrary.wiley.com/doi/abs/10.1002/adma.202301799.
[247] H.-T. Zhou, et al., Hybrid metasurfaces for perfect transmission and customized manipulation of sound across water–air interface, Adv. Sci. 10 (2023): 2207181. https://onlinelibrary.wiley.com/doi/abs/10.1002/advs.202207181.
[248] Z. Huang, et al., Lotus metasurface for wide-angle intermediate-frequency water–air acoustic transmission, ACS Appl. Mater. Interfaces 13 (2021) 53242–53251, https://doi.org/10.1021/acsami.1c16043. PMID: 34704730.